TECHNICAL REPORT

"Assessment of tungsten bricks (intended for the target of the ESS) according to a technical selection protocol agreed with ESS-Bilbao.

Stage 2 results of tests of three batches selected after Stage 1"

Document Code: MT / 120033-2 / 15 / R 02

CONFIDENTIAL

Donostia- San Sebastián

ELABORATED
Javier Aldazabal, Carmen García-Rosales, Javier Gil Sevillano, Amaia Gómez, Antonio Martín Meizoso, Nerea Ordás, José Luis Pedrejón
Date: 01/06/2016

Pº Manuel de Lardizábal, 15

20018 Donostia–San Sebastián Spain

Tel +34 943 212 800 – Fax +34 943 213 076 –
www.ceit.es

CEIT-IK4
Pº Manuel de Lardizábal, 15
20018 Donostia-San Sebastián, Spain
Tel +34 943 212 800 – Fax +34 943 213 076 – www.ceit.es

TABLE OF CONTENTS

1 INTRODUCTION

On account of the results of Stage 1 tests of selection among six tungsten suppliers (report MT / 120033 / 15 / R 01), three of them were retained for another series of tests (Stage 2 of this study): **bricks of reference 2, 5 and 6**. In Stage 2 of the study the microstructure and the residual stress state of the 3 selected materials has been studied in depth and additional mechanical properties have been measured, namely the stress-strain behavior at 400°C and the plane-strain fracture toughness at room temperature.

2 MATERIALS

Properties of the three selected materials for this study can be found in the report of Stage 1. However, supplier no. 5 provided new samples for Stage 2, from the same batch of bricks tested in Stage 1 of our study but now with a polished surface (unspecified polishing method). ESS showed interest in further testing these new samples in Stage 2 instead of the samples no. 5 previously tested in the Stage 1 of the study. In order to check the changes introduced by polishing, the hardness, the residual stress state at the surface and the room-temperature tensile strength (3P bending) of the polished samples has been compared with their corresponding values given in the first report.

Polishing should have no effect on the bulk strength of the tungsten bricks, but one can expect it to have opposite effects on the ductility of the bricks: partial relaxation of the compressive stresses at the surface and of any deformed layer (negative for ductility limited by brittle fracture) and elimination of surface imperfections acting as nuclei of brittle fracture (positive effect).

Vickers hardness (1 kg) measurements were performed on the rolling surface of bricks 5, as received (new samples, polished). The procedure and hardness tester were the same used in Stage 1. The average hardness corresponds to 20 indentations. The results are given in Table1; there is no significant hardness difference between the two batches. The imprints have diagonals of about 70 μm; as the plastic zone under the hardness indenter is about 3 times the size of the imprint, we are sampling a depth of about 200 μm, i.e., we are obtaining a property of the bulk of the specimen, little influenced by the surface layer affected by the grinding/polishing process.

TABLE 1. Vickers hardness (1 kg) of bricks 5

	Vickers hardness (kg mm^{-2})	
	Average	St. dev. p.
5 Stage 1	411.65	16.04
5 Stage 2 (5N)	413.25	20.57

The surface of the new batch under the optical microscope of the hardness tester is manifestly smoother than the surface of the previous batch 5, fig. 1. The aspect of the surface does not allow for assessing the polishing method used; the total absence of scratch lines (confirmed in SEM observations too) points to a possible electro-polishing process.

The {321} X-rays diffraction peak results used for measuring the residual stresses in the as-received surface of the polished (St.2) or ground (St.1) brick 5 is given below, fig. 2 (the measurement procedure and analysis was the same in both cases). Qualitatively, the diffraction spectrum after polishing is similar to the spectrum measured before. Quantitatively, the biaxial residual stress state remains compressive but the absolute value of the two stress components is reduced after polishing, Table 2, as it could be expected.

The relatively narrow double peak of fig. 2, ground or polished brick 5, is very different from the surface diffraction peaks of the other bricks, as was noted in the report of the Stage 1 tests. In figure 3 the surface diffraction peak of batch 2 is shown for comparison, the peaks of the other bricks were qualitatively similar. Such broad peak is associated to a deformed structure, the double peak of brick 5 corresponds to a nearly undeformed material. Indeed, the OM and EBSD observations show that the structure of bricks 5 is recrystallized and very different from the structure of bricks 2 or 6, as explained below in this report.

Table 2. Surface residual stresses, batch 5

Batch 5	σ_L	σ_T
5N, Polished (st. 2)	-111 ± 7 MPa	-170 ± 21 MPa
5, Ground (st. 1)	-247 ± 26 MPa	-230 ± 24 MPa

Three-point bending tests at room temperature were performed as described in the report of Stage 1. However, by mistake the as-received rolling surface of the bricks was placed on the two external supporting cylinders, i.e., in the compressive side of the test; consequently the tensile surface of the samples

corresponded to the EDM machined surface. The behavior was fully brittle fracture intervening without any macroscopic plastic deformation. The results of the maximum tensile stress at fracture are presented in Table 3, where they are compared with the data from the previous material. Unfortunately, the comparison is between the fracture from the as-received surface of the first samples of brick 5 (Stage 1) and the Ceit EDM machined surface. New tests with the current orientation of the samples are in progress.

EDM machining induces a severe decrease of ductility, all measured values of strength being below the 600 MPa limit (compare with fig. 5 of previous report).

Table 3. Tensile strength at room temperature (3PB) of bricks 5 and 5N

Sample 5*	Max. stress (MPa)	Average ± st. dev. p. (MPa)	Sample 5N**	Max. stress (MPa)	Average ± st. dev. p. (MPa)
5 L	788	802 ± 36	5N L	434	382 ± 39
	851			340	
	766			372	
5 T	948	1023.5 ± 83	5N T	395	417 ± 31
	1139.5			461	
	983			394	

**Failure from as-received brick surface* ***Failure from EDM surface*

3 MICROSTRUCTURAL CHARACTERIZATION, INCLUDING SUB-SURFACE POSSIBLE MICROSTRUCTURAL DAMAGE

3.1 GEOMETRICAL DEFECTS AT THE SURFACE AND AT THE INTERIOR OF THE BRICKS

The as-received rolling surface and metallographically prepared LN sections (sections containing the longitudinal and normal direction) of the bricks have been observed unetched in the scanning electron microscope, SEM.

The topography of the surface evidences **dissimilarities in roughness coming from the different finishing processes used by the suppliers** (figure 4-6). The surface of no. 5 is smoother than the surface of the other two bricks; as expected after a polishing treatment. About the nature of such treatment: is it electropolishing? There are no signs of mechanical polishing. Also it seems that the surface of no. 2 is more damaged than the surface of no. 6, but a quantitative characterization would be needed for assessing this claim. There seems to be more material pulled away from the grinding furrows in no.2 than in no.6.

The edges of the LN and NT cross sections have been explored for microcracks or other surface-nucleated defects; the interior, for porosity. Examples of such observations are presented in figures 7-12. The superiority of the surface state (in terms of smoothness and absence of geometrical defects) of brick 5 (polished) is evident. At the surface of brick 6 some folding of the ground subsurface have been detected; again, a more detailed and quantitative characterization should be undertaken for differentiating bricks 2 and 6 with respect to the population of such type of defects. More porosity is detected in brick 2.

3.2 MICROSTRUCTURE

The microstructure of the samples has been revealed by back-scattered electron SEM images and, mainly, by using large-size EBSD-SEM image analysis of LN cross sections, figs. 13-15.

The boldest difference between the three structures of bricks is the recrystallized, bimodal mixture of two equiaxed structures of very different

grain size of no. 5 vs. the deformed (rolled) structures of no. 2 and no. 6. Despite such structural difference, the average grain size of brick 5 is comparable (in fact, smaller) than the grain size of the two other bricks, although the grains of no. 5 are free from subgrains and their appearance is influenced by that fact.

Some surface effects are observed in the grain shapes and orientations very near the surfaces, but those effects are not very pronounced.

The grain sizes measured from the EBSD images are given in Table 4.

Table 4. Grain sizes (LN sections)

Average diameter (by number), μm	No. 2	No. 5N	No. 6
MIDPLANE	24.0 (21.3)	21.3	36.7 (30.2)
SURFACE	34.4 (25.7)	14.1 (8.8)	34.0 (30.9)

Criterion for grain boundaries: 15°. Edge grains included in the analysis. Bracketed: standard deviation p.

The contrast in SEM images using back-scattered (primary) electrons reveal the grain structure. For instance, they show a very thin sub-surface zone affected by the machining (grinding) deformation in brick no. 6, fig. 16a. In figure 16b, the grain distribution in brick no. 5 is bimodal, with the fraction of fine grains being of micrometric size (about 3 μm).

Aligning together EBSD images of the three bricks taken at the same magnification, figs. 17-20, we observe **important structural differences**: besides the obvious fact that no. 5 is recrystallized (partially recrystallized at the surface or, at least, with a high fraction of very small grains recently nucleated), no. 6 has either suffered a larger rolling reduction or its grains are more elongated in the rolling direction because of no. 2 being cross- or clock-rolled (or both). Moreover, the minimum average dimension of the grains (the average size in the short-transverse direction) is more important than the mean (random) grain size with respect to brittle fracture propagation; similarly, the intragranular dislocation substructure has a toughening effect; clean, big grains

are detrimental for brittle fracture nucleation. Both factors go against brick no. 2, although no. 6 has a larger random average grain size. We must, therefore, wait and see the results of the pending tensile and toughness tests for reaching any conclusion.

4 CRYSTALLOGRAPHIC TEXTURE

The crystallographic textures provide us with some additional interesting information about the processing of the bricks. They are shown in figures 21-22.

The differences of symmetry of the direct pole figures indicate that nº 6 was shaped by unidirectional rolling and no. 2 and no. 5N, by cross-rolling (the latter, perhaps clock-rolling). Despite the different (recrystallized) grain structure observed in no. 5N, its texture looks as an inherited deformation texture. The density of {001} planes parallel to the rolling plane at the surface or at the interior of brick 5N is particularly high, i.e., many easy cleavage {100} planes are available perpendicular to the rolling surface in such texture.

5 RESIDUAL STRESSES AT AND UNDER THE SURFACE OF THE BRICKS

X-ray diffraction has been used for measuring the surface and sub-surface residual stress state of the three bricks selected for study in Stage 2 of this project (rolling surface, longitudinal and transverse stresses). The method and equipment were described in the previous report. For sub-surface measurements, successive layers of tungsten were eliminated by electropolishing using a NaOH solution as electrolyte and a graphite anode, after determination of the optimal polishing conditions (room temperature, 1.7-1.8 V, ~70 mA cm^{-2}), and calibration of the rate of depth elimination. As the depths eliminated are very small compared with the brick thickness, no correction for the residual stress field re-equilibration after successive electropolishing stages has been applied to the measured lattice strains and stresses. Sub-surface has been characterized until about 100 μm.

The results are summarized in Table 5 and figs. 23 and 24.

The stress state is near-balanced biaxial in all cases but clear quantitative differences are evident between the three bricks. In ref. 5N, the double, narrow peak at any depth indicates a recrystallized structure. The other two bricks show wide single peaks near the surface that narrow and become double as depth below the surface increases; they are still wider than the peak of brick 5N even below 100 mm, an indication of their deformed structural state (as SEM-EBSD observations confirm). **The stress state at the free surface is compressive in all cases, but the absolute value of the stresses is very weak for brick 5N and maximum for brick 2**.

The compressive stress state disappears at depths 15, 40 and > 100 μm for respectively bricks 5N, 6 and 2.

The heavily deformed layer (responsible for the widening of the peaks is irrelevant for brick 5 and is about 40 μm for bricks 2 or 6.

6 TENSILE STRENGTH AND DUCTILITY AT 400°C (3-POINT BENDING TESTS), L AND T DIRECTIONS

Bending tests in air at 400°C were performed as described in the technical report of Stage I of this study. Unfortunately, the same error in the position of the samples, described in section2 (above, this report) was made for all the bending tests at 400°C. We thus have not tested the as-received surface in bending, as intended, but the EDM machined surface. The results are comparable among them and correspond to a "worst case" behavior: in air at 400°C with tension applied in the rough, heavily damaged surface obtained by electro-discharge (EDM) machining. Despite that, **in all cases but for orientation T of brick 6, the behavior is above the DBT temperature**, with considerable plastic deformation before fracture, although fracture itself occurs by brittle mechanisms (mixture of intragranular cleavage and intergranular decohesion).

A summary of the maximum apparent strengths recorded is given in Table 6 and figure 25. The maximum stress in bending has been calculated with the formula valid for elastic bending,

$$(\sigma_{max})_{elastic} = \frac{3F_{max}L}{2bd^2} \quad (1)$$

The absolute values given in the table are thus not valid true stress values, as there is plastic deformation even in the less ductile case (orientation T of brick 6). The values are only meant for comparison between the three bricks. For elastoplastic bending of a non-hardening material, the limit (asymptotic) load would be

$$F_{max} \rightarrow \frac{3F_y}{2} \quad (2)$$

On account of plastic strain hardening, in our case,

$$(\sigma_{max})_{apparent} \geq \frac{3\sigma_y}{2} \quad (3)$$

The apparent stress-strain behavior of bricks 5N and 6 is shown in figure 26[1]. The yield stresses (elastic limit) are about 600 MPa, 800 MPa and 1000 MPa for, respectively, samples 5N (mixed orientation L or T), 6L and 6T. The tensile strength levels are not much above the limit strength expected from perfect plasticity (eq. 2).

Pictures of the broken bent specimens are shown in fig. 27. The poor ductility of bricks 6T relative to bricks 2 or 5 of any orientation is evident. Such relative poor ductility is not related with the surface state; the anisotropy of the fracture stress is rather similar in the tests performed at room temperature: the ratio of the failure stresses L/T is 2.3 at room temperature (original surface of the bricks) and 1.7 at 400°C (EDM surface).

The fractography of different samples is displayed in figs. 28-33. Testing in air at 400°C has produced some surface oxidation. Qualitatively, it seems that the fraction of intergranular decohesion is the smaller for sample 2, where cleavage prevails and the fracture surface is rougher.

Tests with the correct position of the surface under tension are under way.

[1] The stress-strain curves of samples no. 2 were accidentally lost, only the maximum strength was recorded.

7 FRACTURE TOUGHNESS AT ROOM TEMPERATURE

The plane-strain fracture toughness of the samples has been measured at room temperature by using chevron-notch ("Barker") specimens according to ASTM E1304-97 (Reapproved 2008) standard. The advantage of this method is that it does not require fatigue pre-cracking of the specimen, particularly interesting for tungsten (or any brittle material in general); the tests measures the critical stress intensity factor for crack propagation. Square-section rod specimens 10x10 mm^2 with a length to width ratio W/B = 2 have been used (figure 34), machined by EDM; as the brick thickness is 10 mm, the crack propagation occurs at the midplane of the bricks for SL orientation (short-transverse loading direction, longitudinal crack propagation direction) or across the plane normal to the longitudinal direction in the transverse direction for the LT orientation (loading in longitudinal direction, crack propagation in the transverse direction). The toughness for SL orientation represents crack propagation under bending around the transverse direction, T; that corresponding to LT orientation, to bending around the S direction. These two orientations have been chosen as the most representative thermomechanical loading modes for the bricks in the ESS target operation (bricks in vertical position with the two TS basis inserted in grooves).

The load vs. mouth-opening displacement curves are mostly of the smooth crack growth type, although some curves show small jumps. In some cases, unloadings were made for checking the possibility of using the method based on loading-unloading cycles (the brittleness of the samples makes difficult to use the loading-unloading method). The results are presented in fig. 35.

As the pure tungsten tested is rather brittle, the plane-strain fracture toughness has been calculated using only the maximum load, P_M. The critical stress intensity factor is (conditioned to the requirements for validity, see ineqs. 5 and 6, below),

$$K_{QnM} = \frac{Y_M^* P_M}{B\sqrt{W}} \qquad (4)$$

The coefficient Y_M* is, for the geometry used, 29.90. The maximum loads are displayed in fig. 36.

All values of $K_{Q\nu M}$ comply with the required ASTM 1304-97 conditions for the sample geometry used (square section, B = 10 mm, W/B = 2, slope ratio of load-mouth opening curve r_c = 0.30, yield stress $\sigma_{YS} \approx HV/3 > 1160$ MPa):

$$B > 1.25 \left[\frac{K_Q}{\sigma_{ys}}\right]^2 \quad (5)$$

$$r_{P_M} > 1.2 r_c = 0.46 \quad (6)$$

Consequently, they can be considered valid $K_{I\nu M}$ plane-strain fracture toughness values. They are given in Table 7 and fig. 37.

The toughness anisotropy is considerable. In the three cases the toughness for crack propagation parallel to the rolling plane is smaller than for propagation normal to the rolling direction, as it could be expected from the grain shape anisotropy (both for cleavage and for intergranular decohesion the most favorable propagation paths are along the rolling plane). **Bricks 5N have the lowest toughness of the three tested materials, bricks 2 have some advantage over bricks 6.**

Table 5

Summary of measurements of evolution of sub-surface residual stresses

Depth		Surface			~ 5 µm			~ 14 µm			~ 33 µm			~ 55 µm			~ 110 µm		
Supplier	Stress	RS (MPa)	StdDev	Depth	RS (MPa)	StdDev	Depth (µm)	RS (MPa)	StdDev	Depth (µm)	RS (MPa)	StdDev	Depth (µm)	RS (MPa)	StdDev	Depth (µm)	RS (MPa)	StdDev	Depth (µm)
2	σ_L	-789	11	0	-648	11	6	-614	13	14	-357	9	33	-152	8	55	-57	2	107
	σ_T	-1088	9	0	-955	10		-781	8		-480	8		-185	8		-77	10	
5N	σ_L	-111	7	0	-34	12	5	-4	8	14	-5	13	33	6	20	58	3	11	107
	σ_T	-170	21	0	-58	16		-13	9		-22	13		-2	9		-12	9	
6	σ_L	-709	18	0	-657	14	5	-497	14	13	-74	11	33	1	100	56	28	18	113
	σ_T	-1055	7	0	-850	27		-551	16		-68	11		85	125		96	22	

***Table 6**. 3P bending tests at 400°C in air. EDM surface. Maximum stresses calculated assuming elastic bending ($\sigma_{max} = 3F_{max}L/2bd^2$)**

	σ_{max} (apparent), MPa					
	2		5N		6	
L	1579 1463	1521	1220 1254 1319	1237	1462 1729 1570	1587
T	1541 1365	1453	1220 1173		946 947 900	931

** The stress-strain behavior is elasto-plastic, i.e., the stress values shown in the table are only valid for internal comparison of the three bricks. One specimen of each material and orientation broke accidentally during test preparation; the orientation of the specimens of brick 5N was lost; however, no difference of behavior could be distinguished for the two orientations tested, the 5 valid results do not show more dispersion than the results of each different orientation of the other bricks.*

***Table 7**. Plane strain fracture toughness from chevron-notch specimens*

K_{IvM} (MPa $m^{0.5}$)				
	SL	SL average	LT	LT average
2	15.31	18.06	23.76	22.64
	14.76		22.35	
	24.10		21.81905	
5N	11.52	12.27	26.41	21.02
	11.97		25.75	
	13.32		10.91	
6	19.87	16.74	21.71*	22.29*
	15.37		22.07*	
	14.99		23.09*	

**Invalid values, crack deviation.*

The absolute values of the toughness and the anisotropy pattern found agree reasonably well with published values for forged or rolled pure tungsten bulk polycrystals. We have made a review of the literature on the fracture toughness of tungsten, it is summarized in Table 8. Our values obtained using the chevron-notch specimens appear to be on the upper side of the published values for polycrystals. They are also compatible with the range of fracture toughness anisotropy at RT of differently oriented W single crystals is 6.2-20.2 MPa $m^{0.5}$ (Gumbsch, 2003), considering that the presence of grain boundaries enhances the brittle toughness.

Pictures of the broken fracture toughness samples are presented in fig. 38. The orientation influence on the type of fracture is evident:

- all specimens with SL orientation but one (2 SL 3) fail by planar fracture guided by the notch, without any deviation.
- by contrast, all LT specimens by one (5N LT 3) fail by arm fracture deflection;

Arm fracture occurs after considerable propagation in the notch plane and only when the load surpasses 1 kN. Consequently, it is related to a high resistance to crack propagation.

This is also true when crack deflection occurs in specimen 2 SL 3. In this specimen crack deviation only takes place when the crack front is larger than B/3, i.e., its toughness value is valid according to ASTM E1304. The same is true for 2 LT and 5N LT specimens, but not for 6 LT ones, they fail by arm cracking before their crack front reaches B/3 width, their apparent toughness values being thus invalid, as indicated in Table 7.

The early arm fracture of specimens 6 LT indicates an easy fracture path in TL orientation relative to specimens 2 LT and 5 LT; such relative weakness is coherent with the results of bending at room temperature, fig 5 of report of Stage 1 of this study. It could be related with differences in crystallographic texture (there is a weak maximum of {001} cleavage planes in T direction in the midplane of bricks 6 that is not present in their L direction, fig. 22; it is absent in bricks 2. It is present in bricks 5N, but their failure occurs mainly by intergranular decohesion).

8 FINAL COMMENTS

For a semicircular crack of radius *a* perpendicular to a semi-infinite plate, under remote tensile stress, a situation approximate to the cracking of a brick from a small surface crack, the stress intensity factor is given by

$$K_I \cong 1.26\sigma\sqrt{a} \qquad (7)$$

At room temperature, our most brittle material (5N L) fails in bending when the maximum tensile stress at its surface is about 400 MPa (Table 3), neglecting its surface residual stress (compressive, -170 MPa, Table 5) that quickly reduces to zero at 10 μm under the surface (fig. 23a). Its measured critical stress intensity factor is K_{Ic} = 12.3 MPa $m^{0.5}$ (Table 7). For a fully brittle fracture (linear elastic state) tungsten 5N would require, according to eq. (7) the presence of a semicircular crack of 590 μm perpendicular to its surface and to the longitudinal direction (and this is still a lower bound, because the fracture test was performed in bending). Its characteristic structural length is 14 ± 9 μm (grain size, Table 4), more than an order of magnitude smaller than the previously mentioned critical crack length on the assumption of linear elastic fracture. **As it happens with other brittle fracture of metals (e.g., ferritic steels below their DBT), the fracture of polycrystalline tungsten is locally preceded by plastic deformation and some concatenation of brittle microfracture events triggered by dislocation activity.**

9 CONCLUSIONS

- The boldest conclusion of this study, important for any application of commercially pure tungsten when thermomechanical failure at low or moderate temperatures is an important design criterion, is that striking differences in structure and mechanical properties (particularly in their anisotropy) can be measured in batches from different suppliers despite all of them having received similar requirements. Tightening of these requirements is thus necessary for avoiding future risks.
- Bricks no. 5N possess a structure completely different from the structures of bricks 2 or 6. It is a recrystallized bimodal structure with two populations of equixed grains free from dislocation contents and wildly differing in grain size. The fine grain fraction is scarce in the brick interior but amounts to about 50% at the surface.
- The structure of bricks 2 and 6 is a typical structure of rolling deformation, as attested by their oriented morphology. Probably they have been stress relieved below their recrystallization temperature but their grain interiors retain an important deformation substructure of dislocations, evident in the EBSD-IP images and in the EBSD images of quality. Such structure was the one specified to the suppliers, because it enhances the brittle fracture toughness with respect to recrystallized structures of similar grain size.
- The plane strain fracture toughness (crack propagation) of the three bricks selected after Stage 1 of this study is rather similar (toughness value and anisotropy). Bricks 2 show a weak advantage in terms of both average values and dispersion.
- There are important differences in the residual strain pattern between the three bricks. Residual stresses are negligible for bricks 5N, which were polished and thus, devoid of their original surface distorted by machining and grinding. Bricks 2 and 6 show important biaxial compressive stress states at the surface, their absolute value decreasing below the surface; bricks 2 retain such compressive state until depths of about 100 μm, bricks 6 only until depths of 40 μm. The depth covered by the compressive state is much larger than the grain size measured in the short-transverse direction in both cases, i.e., the residual stress pattern will be of importance for the tensile

strength of the bricks under bending stresses (under any circumstance where the failure nucleates from the surface of the bricks).

- Bricks 2 outperform bricks 6 in bending behavior at room temperature (report Stage 1). At 400°C and with samples with surfaces machined by EDM, bricks 2 outperform both bricks 6 and bricks 5N. The anisotropy of tensile strength is the highest of the three batches for bricks 6, which show lack of ductility in one of the orientations tested.
- Considering the whole characterization study performed, bricks 2 are, in our opinion, from a technical point of view, to be preferred for the application among the supplied lots of bricks.

Note: tests at 400°C with the as-received surface in the tensile side of the bending samples are in progress.

Table 8. Review of published values of fracture toughness of pure bulk polycrystalline tungsten.

Bulk polycrystalline pure W. Fracture toughness at room temperature, K_{Ic} (MPa $m^{0.5}$)				
Reference	Undeformed OR recrystallized	Comments	Deformed state	Comments
Babak (1983)	7.5	Rex.at 2000ºC	28.5	Unspecified
Margevicius (1999)			8 (T or.)	Swaged rod
			12.6 (L or.)	
Gumbsch (2003)			8 (T or.)	Swaged rod, 65% red.
			19.5 (L or.)	
Faleschini et al. (2007)			4.4-5.4	Rolled, 60% red.
			5.4	Rolled, 80% red
			~ 30	SPD (HPT)
Rupp et al. (2009)			7 (T or.)	Rolled, 65% red.
Rupp et al. (2010a)			14.5 (L or.)	Rolled rod, 65% red.
Rupp et al. (2010b)			8.1 (RL)	Rolled rod, 65% red.
			13.4 (LR)	
Gludovatz et al. (2010)	5.1	As sintered	4.7 (CR or.)	Rolled rod, 84.7% red.
			9.1 (LR 0r.)	
			5.4 (LR or.)	Id., 97% red.
			35.1 (LR or.)	Id. + wire drawing, 99.8% red.
Gludovatz et al. (2011)	~ 8	As sintered	5-15	Rolled rod, anisotropy range
	~ 11	Hipped		
	~ 5	Recrystallized		
Gludovatz et al. (2013)	3-5 (crack prop. Initiation)	Recrystallized, 2000ºC, 1 h	~ 8 (crack prop. Initiation)	Forged bar
	~10 (extended crack prop., R-curve behaviour)		~10 (extended crack prop., R-curve behaviour)	

Note: L, T refer to longitudinal or transverse oriented 3P bending tests of rods. CR, LR or RL, to DCB or CT specimens respectively loaded in circumferential, longitudinal or radial direction, with the crack growing in radial or longitudinal direction. The fracture micromechanisms at RT are brittle; the fracture surface is mainly due to transgranular cleavage, with always some proportion of intergranular decohesion fracture surface.

10 FIGURES

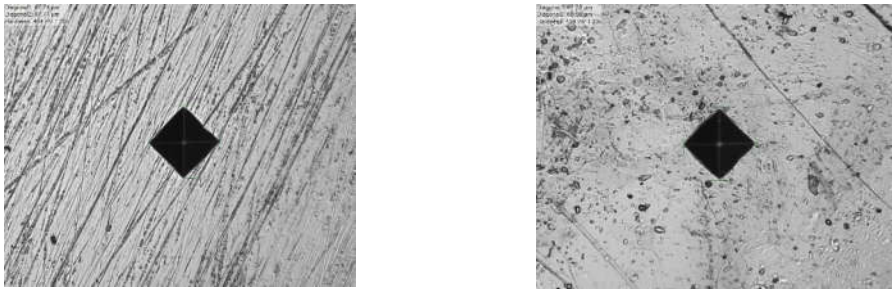

***Figure 1**. Example of indentations on the rolling surface of brick 5; stage 1 (left), stage 2 (right).*

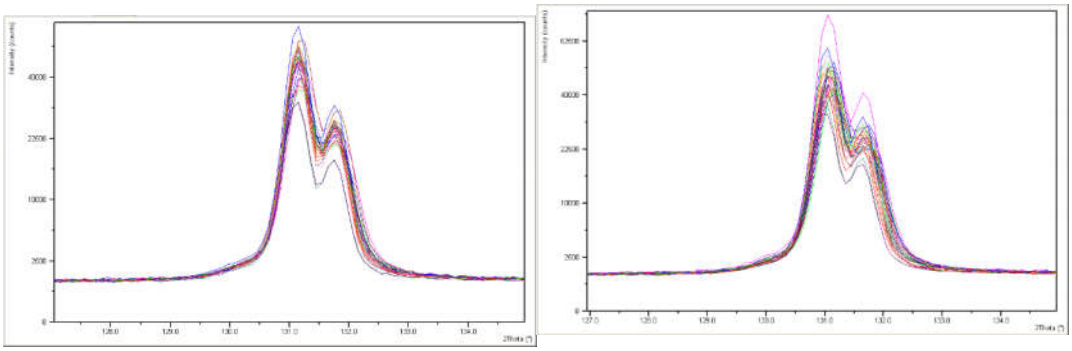

***Figure 2**. Diffraction spectra from surfaces of brick 5N, polished, left and 5, ground (?), right.*

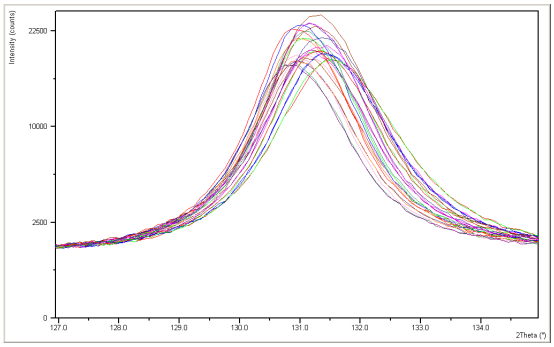

***Figure 3**. Diffraction spectrum from the surface of brick 2 (Stage 1).*

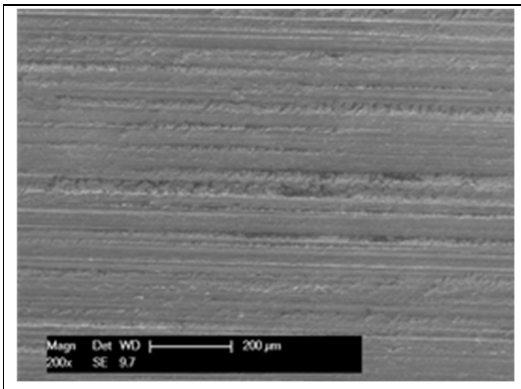

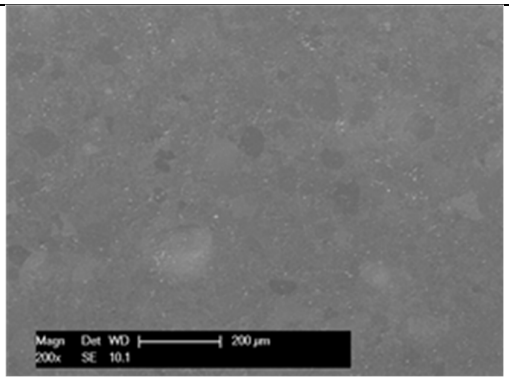

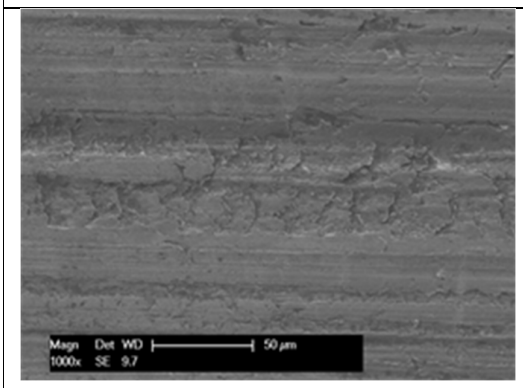

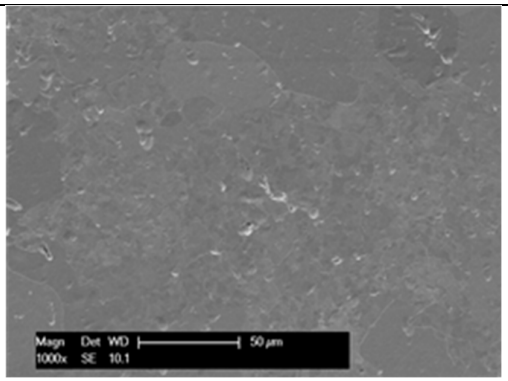

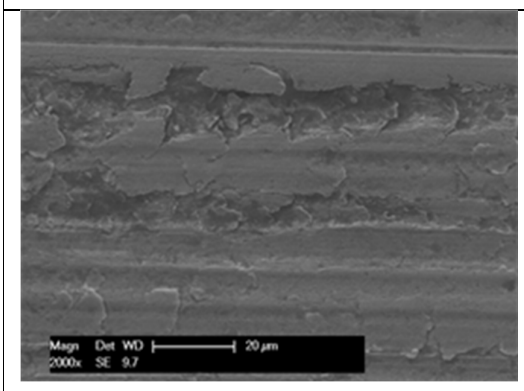

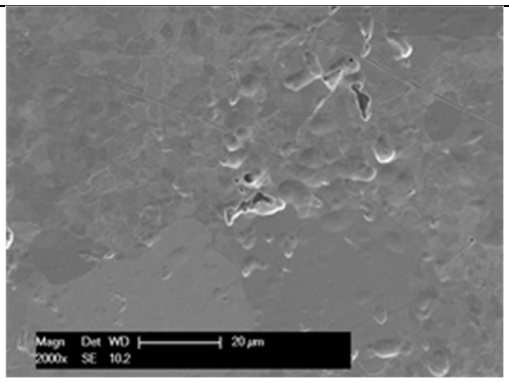

***Figure 4**. Rolling surface, brick 2.*

***Figure 5**. Rolling surface, brick 5.*

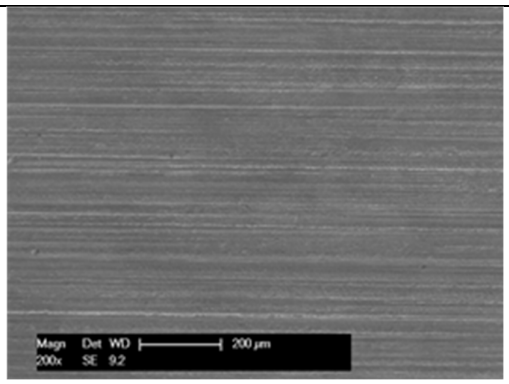

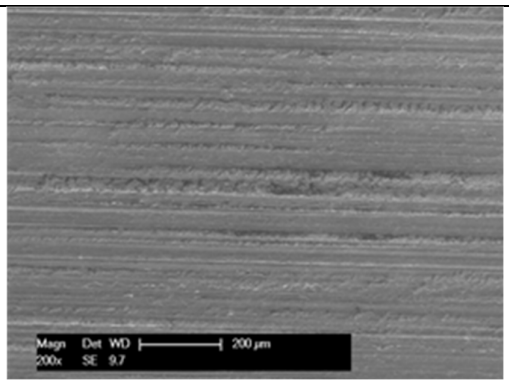

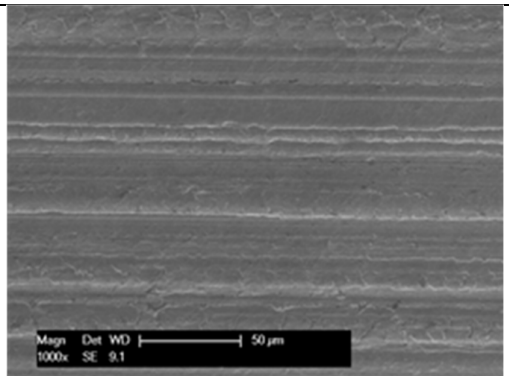

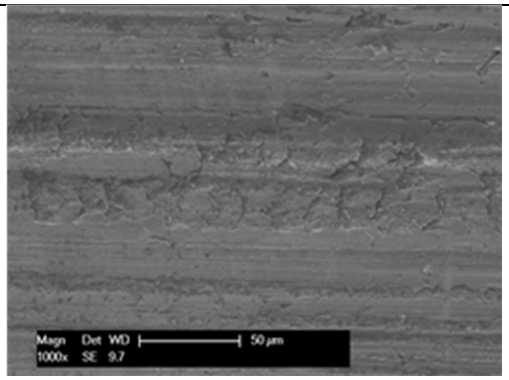

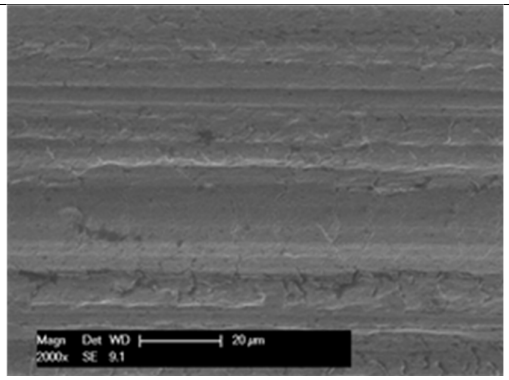

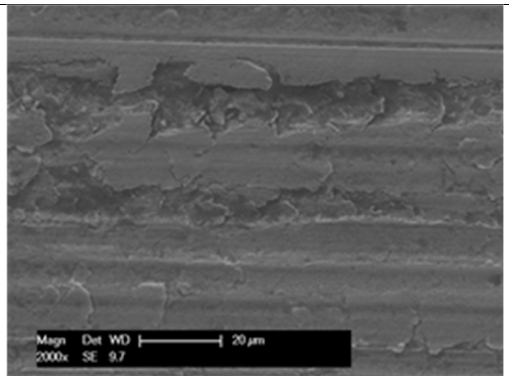

***Figure 6**. Rolling surface, brick 6*

***Figure 4** (repeated). Rolling surface, brick 2.*

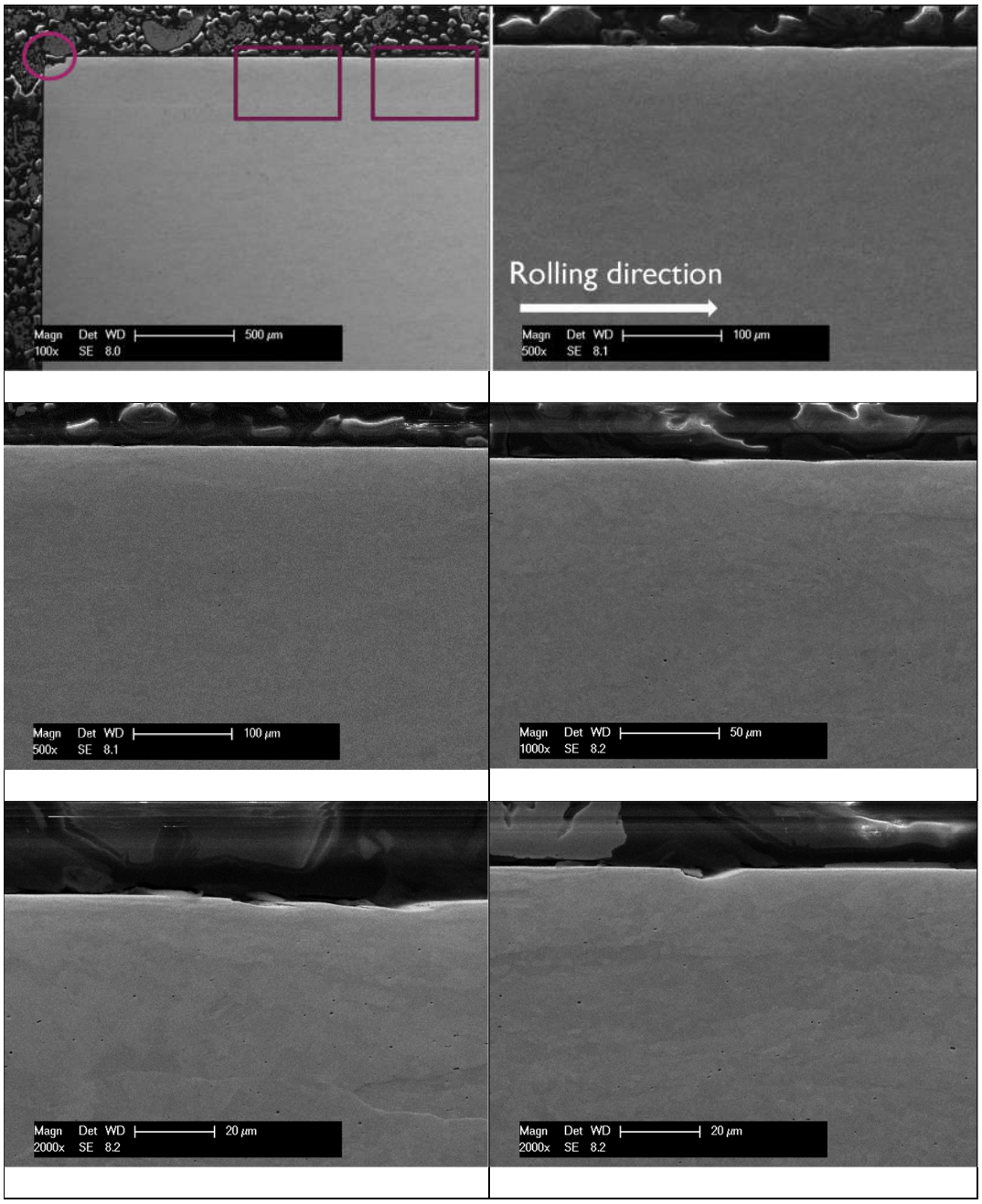

***Figure 7**. Brick 2, unetched, LN section, SEM secondary electrons images.Encircled in the corner of the first image, damage induced by cutting the sample.The edge is free from microcracks, some shallow defects probabli associated with the grinding relief observed in fig. 4. Nanoporosity can be seen at high magnification (the two figures at the bottom).*

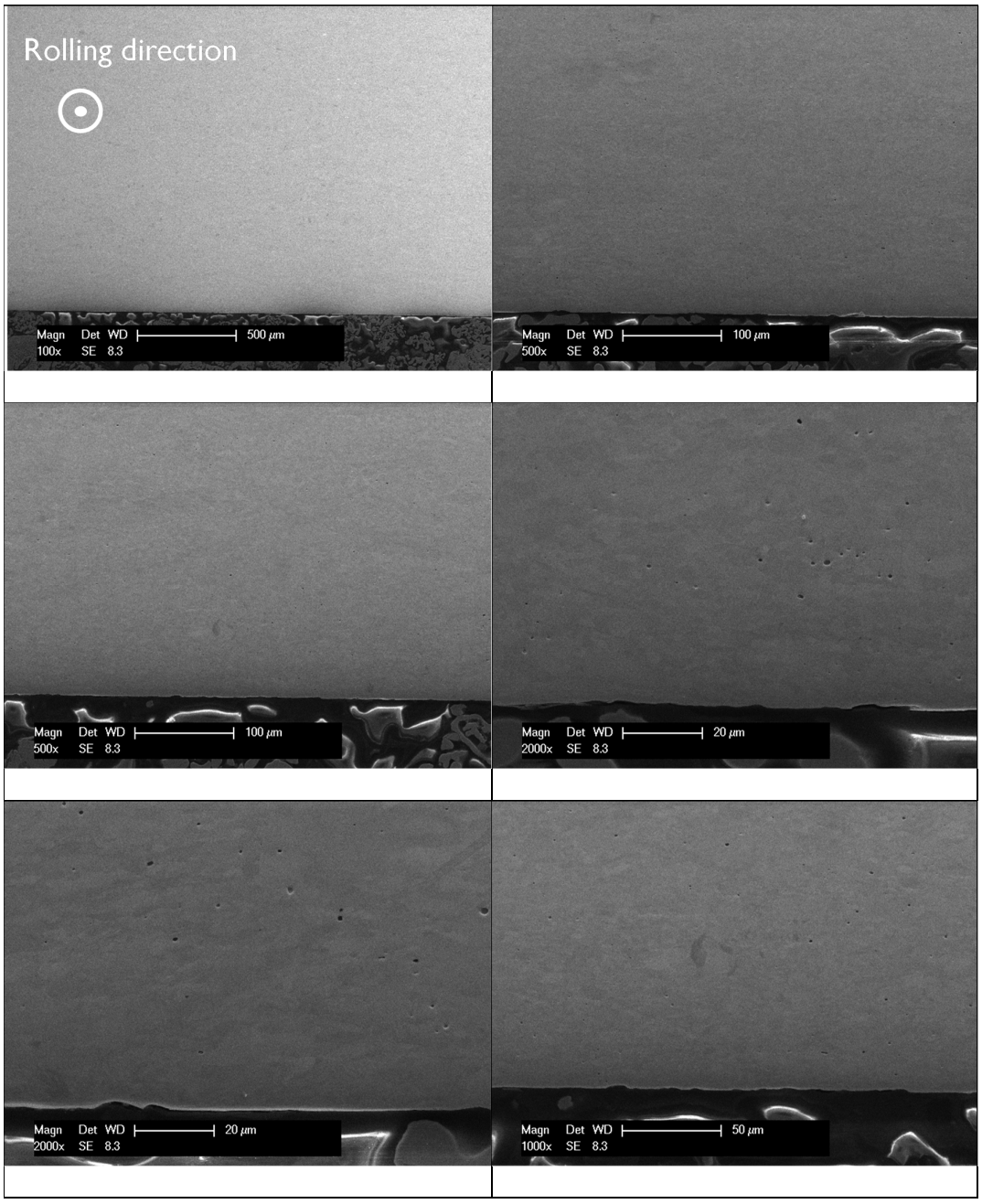

***Figure 8**. Brick 2, unetched, NT section, SEM secondary electrons images.*

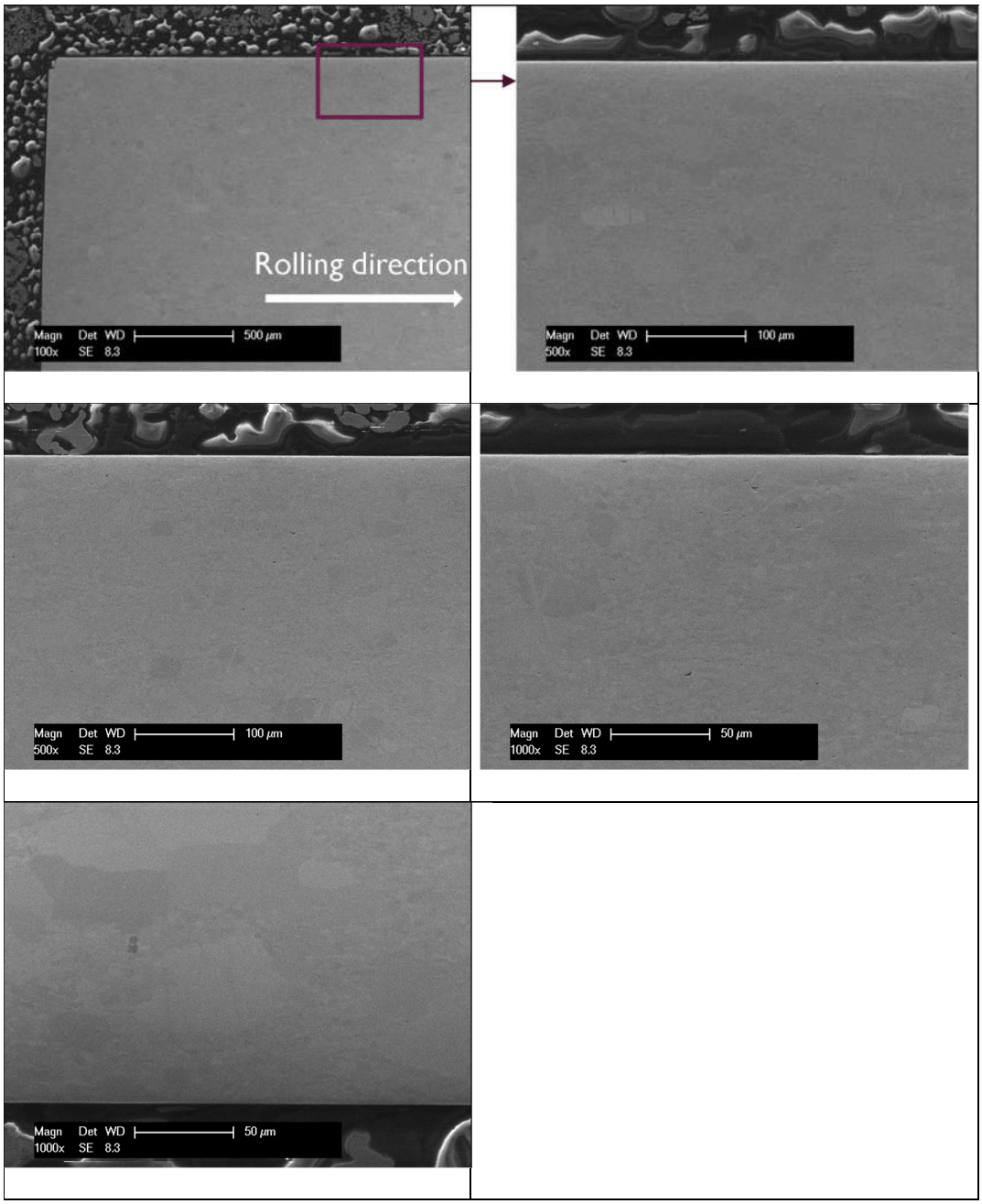

***Figure 9**. Brick 5, unetched, LT section, SEM secondary electrons images.*

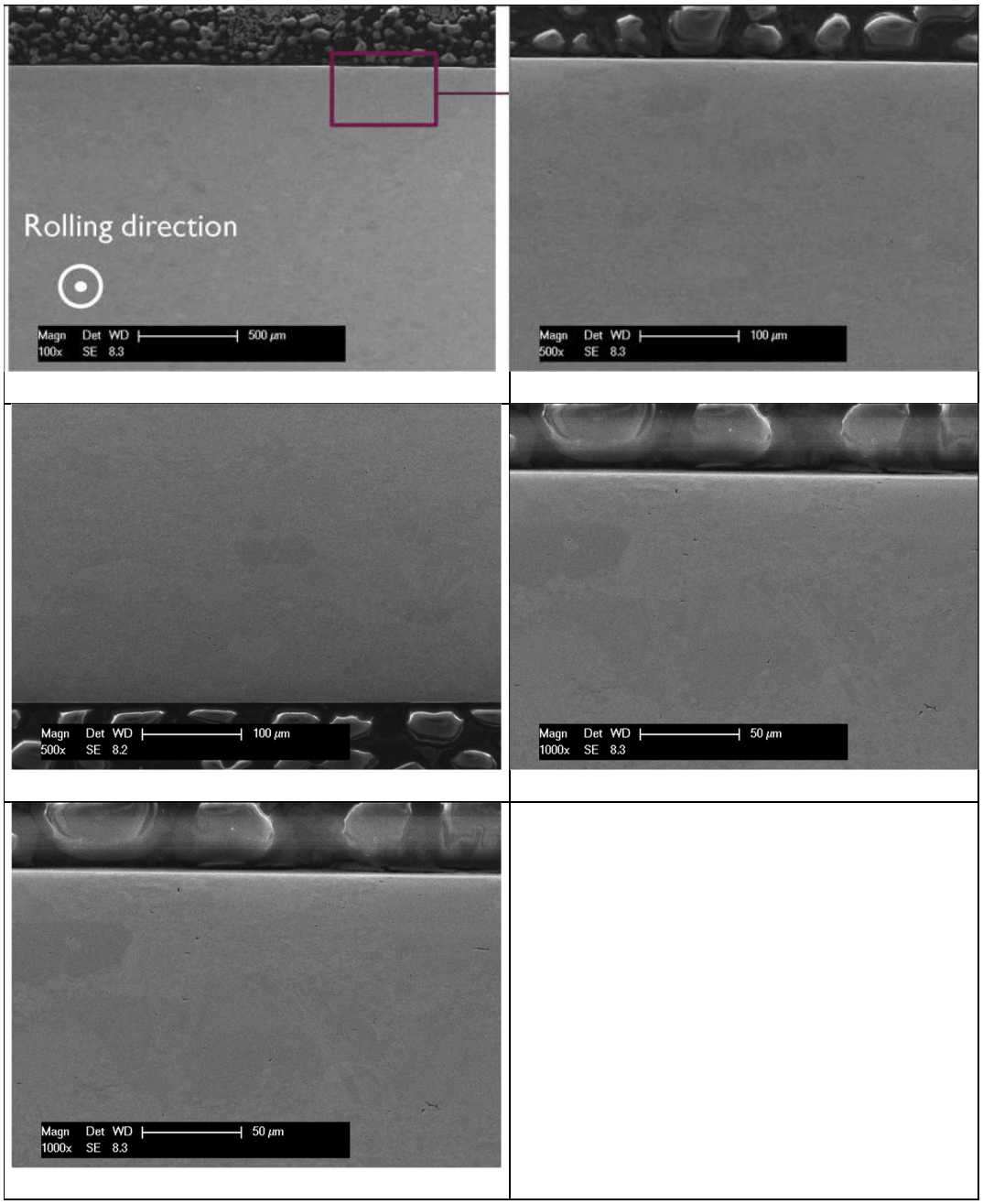

***Figure 10**. Brick 5, unetched, NT section, SEM secondary electrons images.*

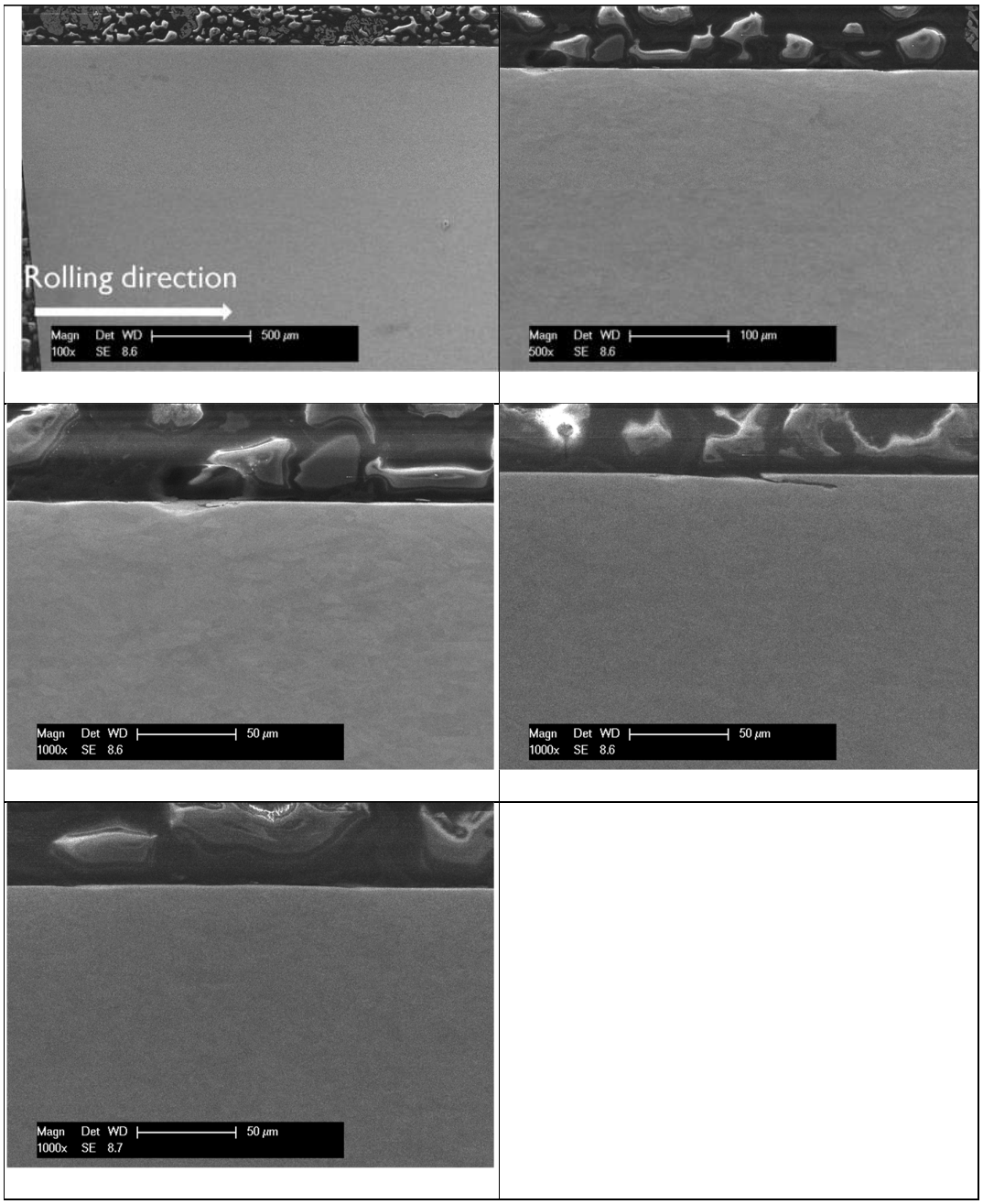

***Figure 11**. Brick 6, unetched, LN section, SEM secondary electrons images.*

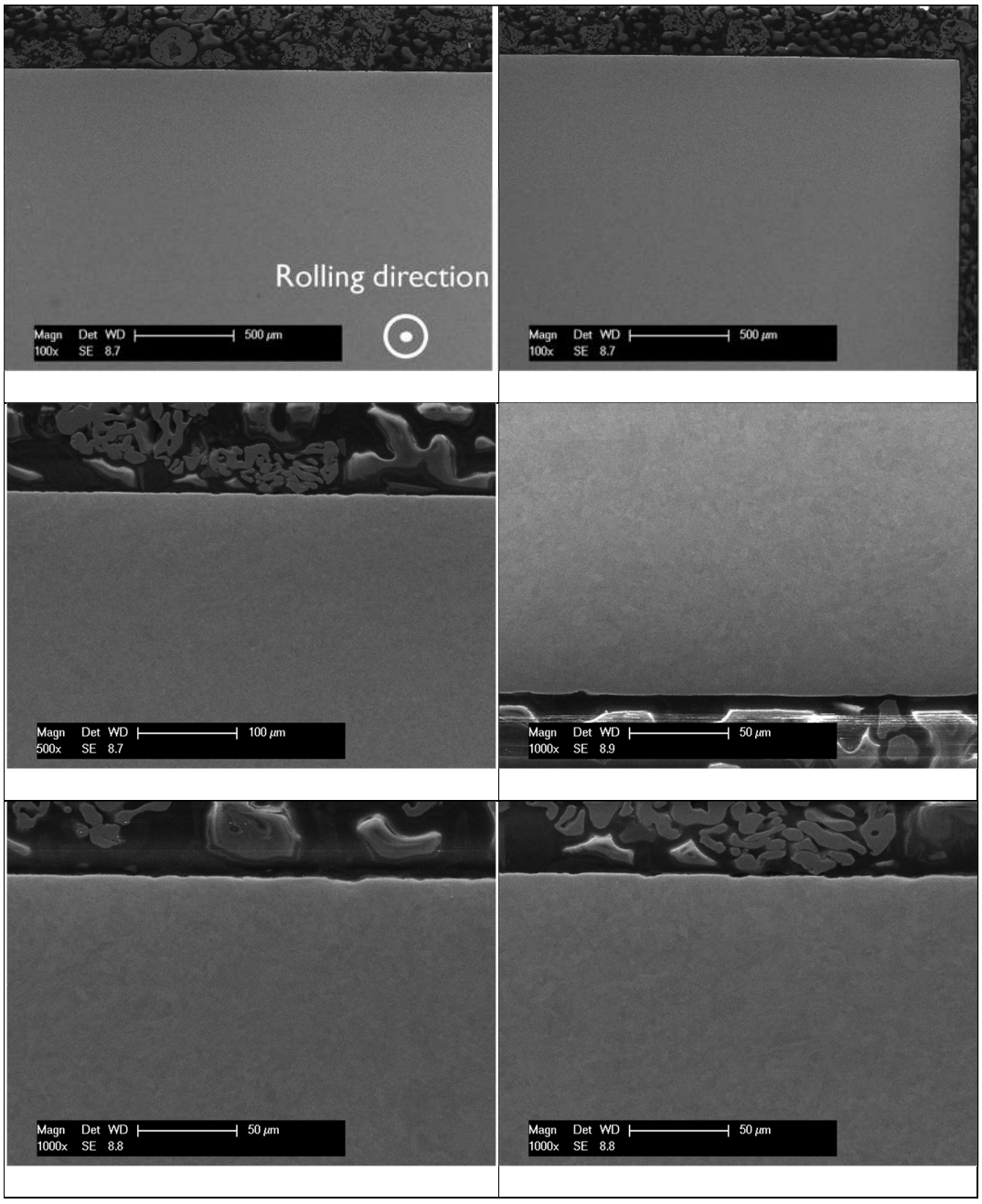

***Figure 12**. Brick 6, unetched, NT section, SEM secondary electrons images.*

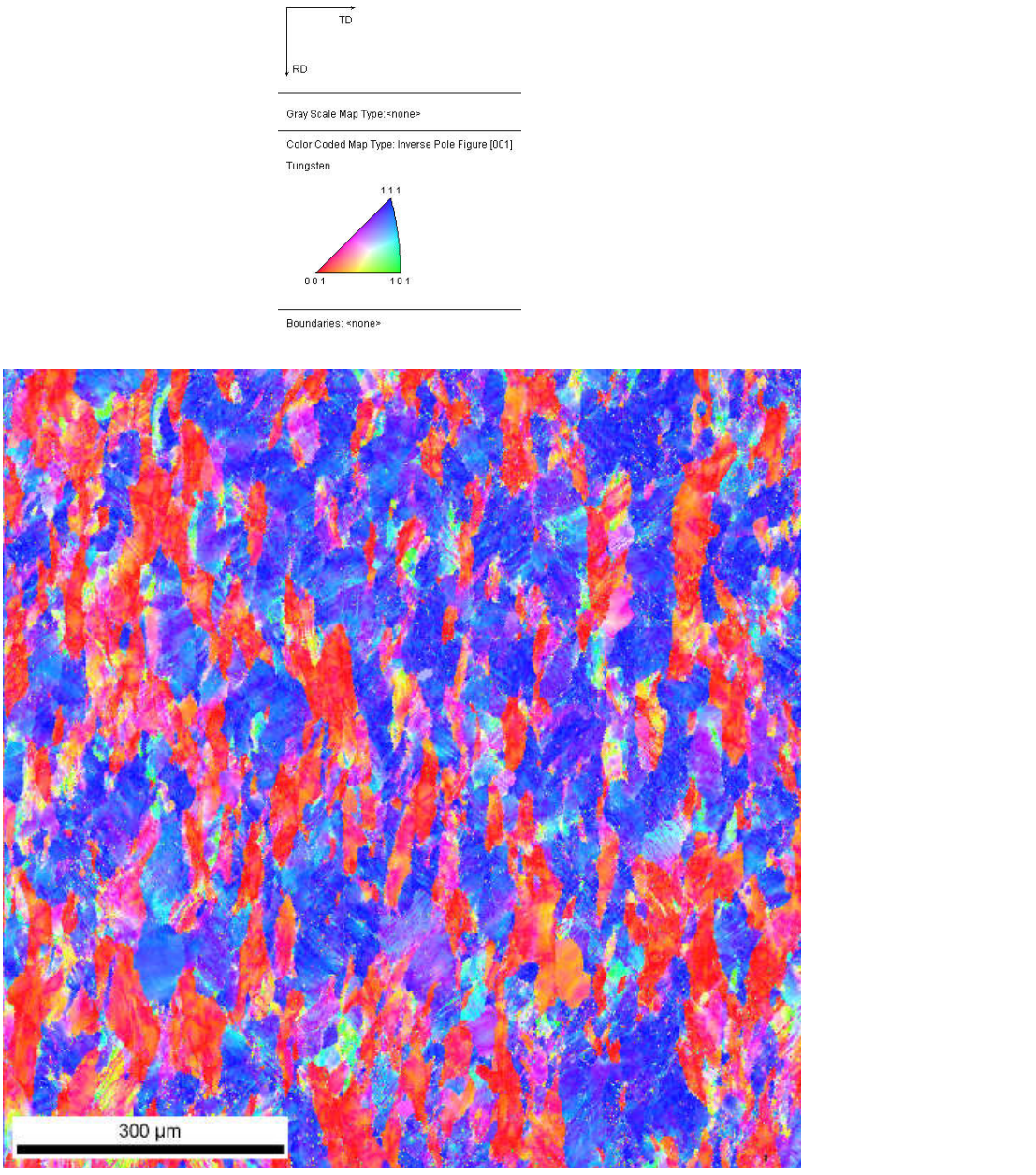

Figure 13a. Brick 2, LN section (rolling direction L is vertical), midplane, IP-coded image with respect to the rolling plane normal (N direction).

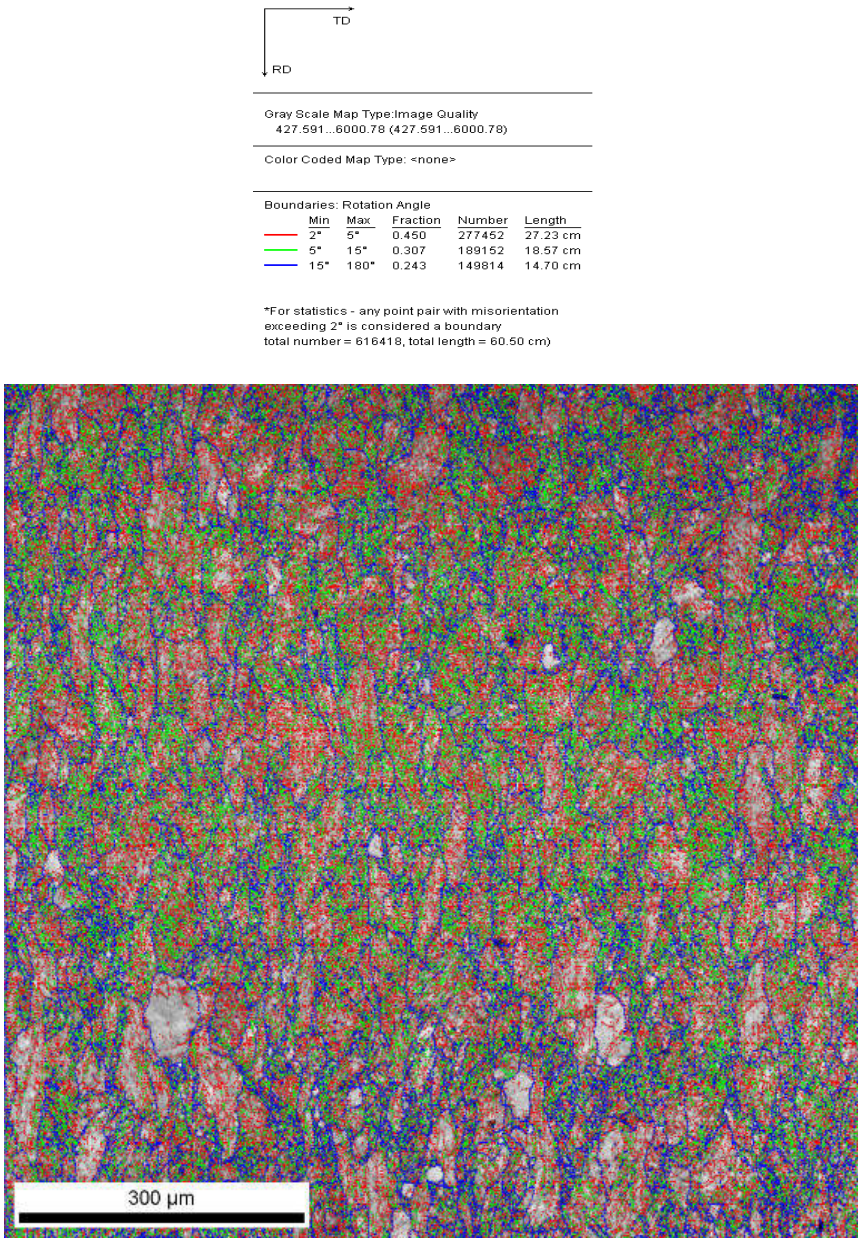

***Figure 13b**. Brick 2, LN section (rolling direction L is vertical), midplane, grain boundaries (blue lines) and sub-boundaries (lines green and red) superposed on image quality (gray scale).*

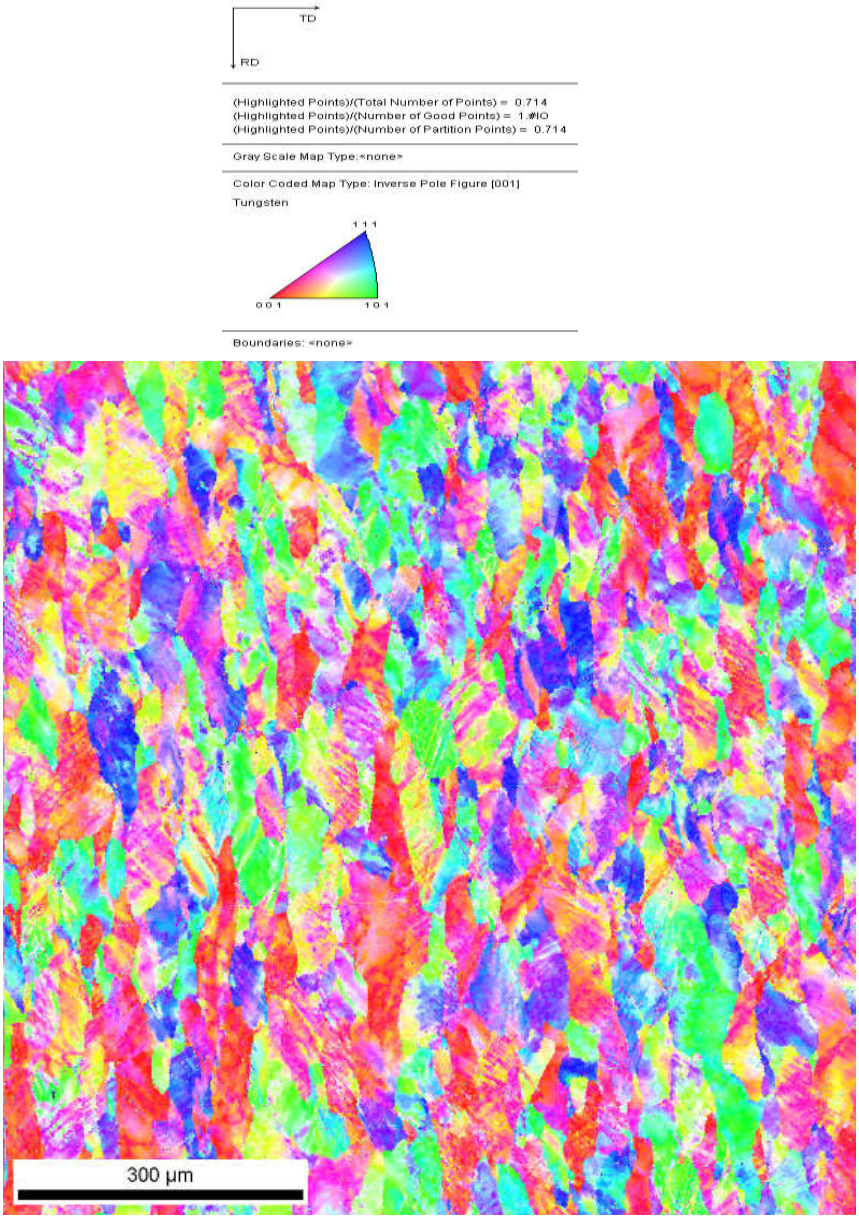

***Figure 13c**. Brick 2, LN section (rolling direction L is vertical), surface. Edge is close to the left of the picture.*

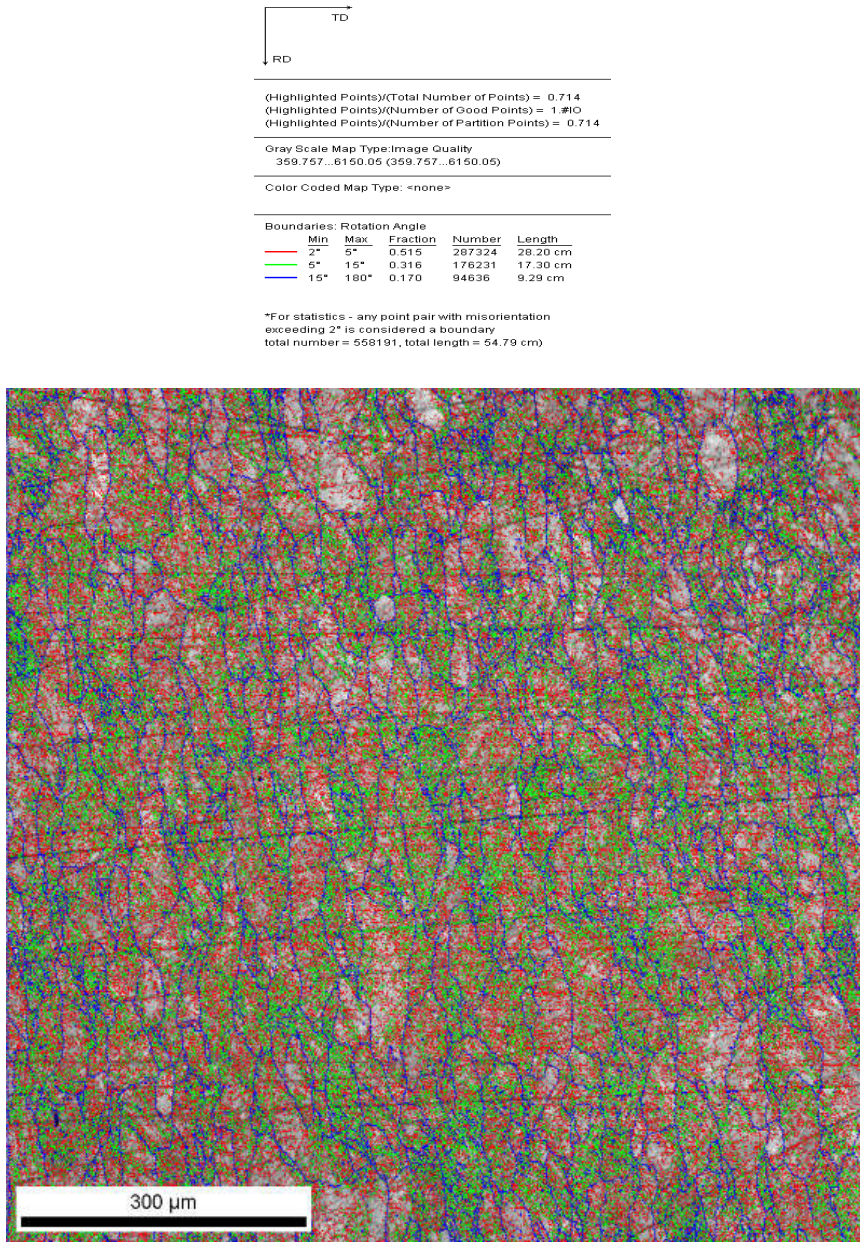

***Figure 13d**. Brick 2, LN section (rolling direction L is vertical), surface.*

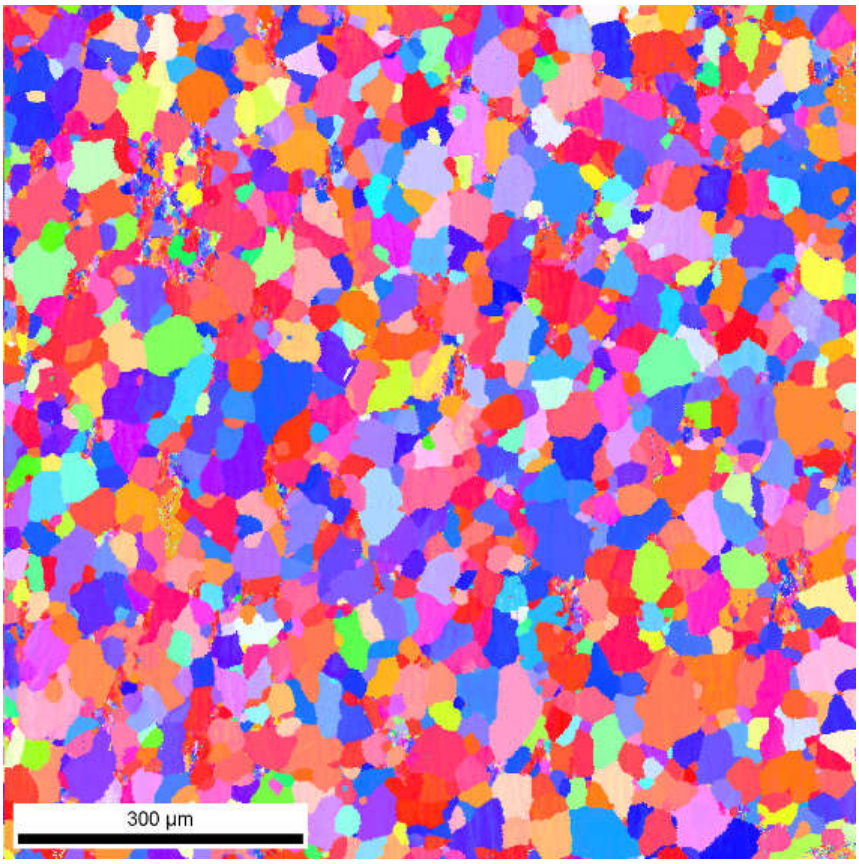

***Figure 14 a**. Brick 5N, LN section (rolling direction is vertical). Midplane.*

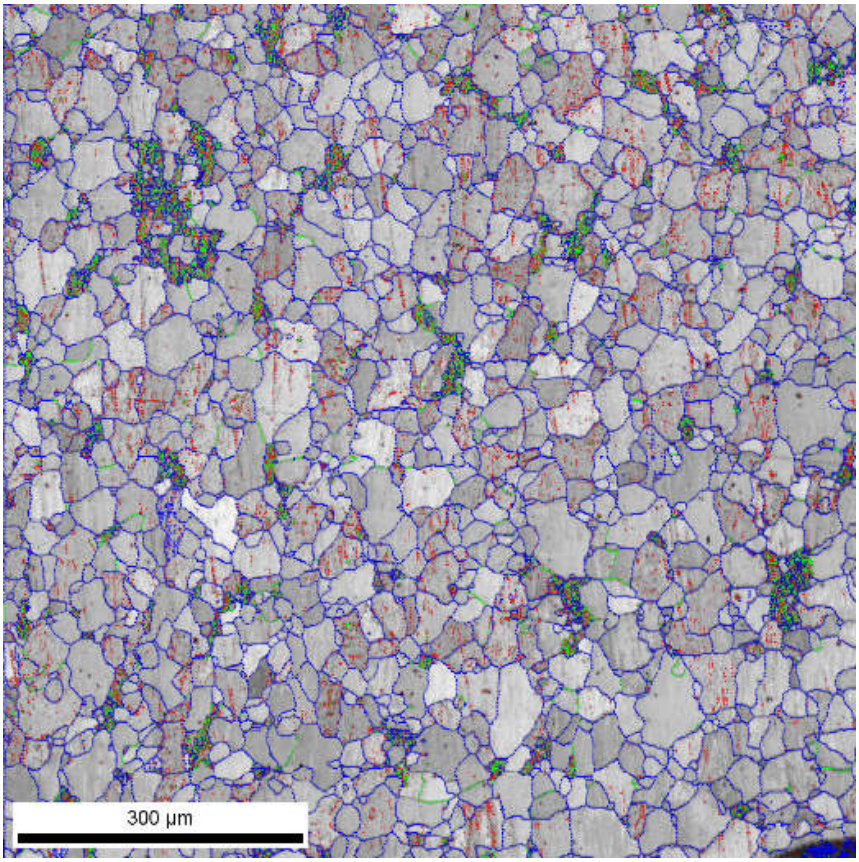

***Figure 14b**. Brick 5N, midplane. Bimodal grain size distribution with small fraction of fine grain size regions. Grain interiors nearly devoid of deformation substructure.*

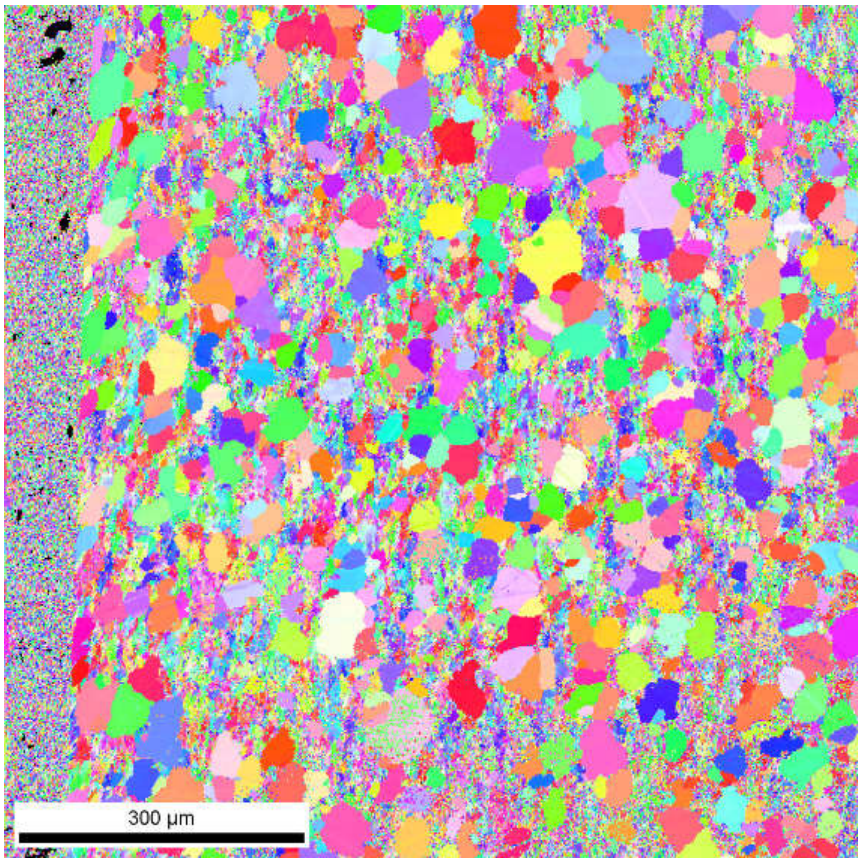

***Figure 14c**. Brick 5N, surface. Left mottled edge band is the embedding mounting resin.*

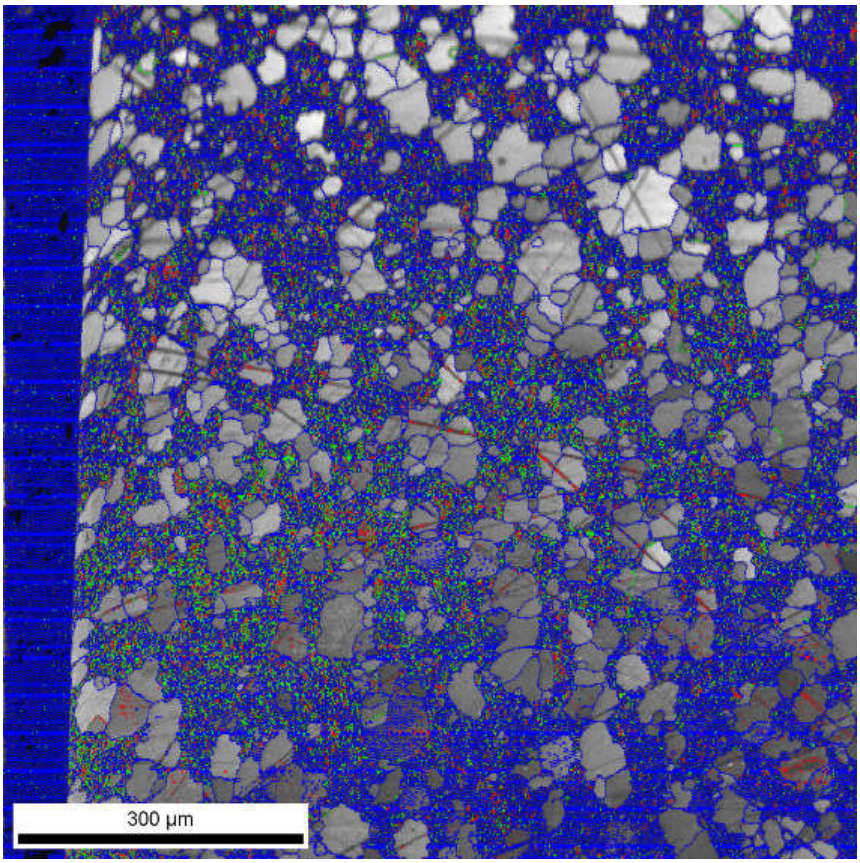

***Figure 14d**. Brick 5N, surface.*

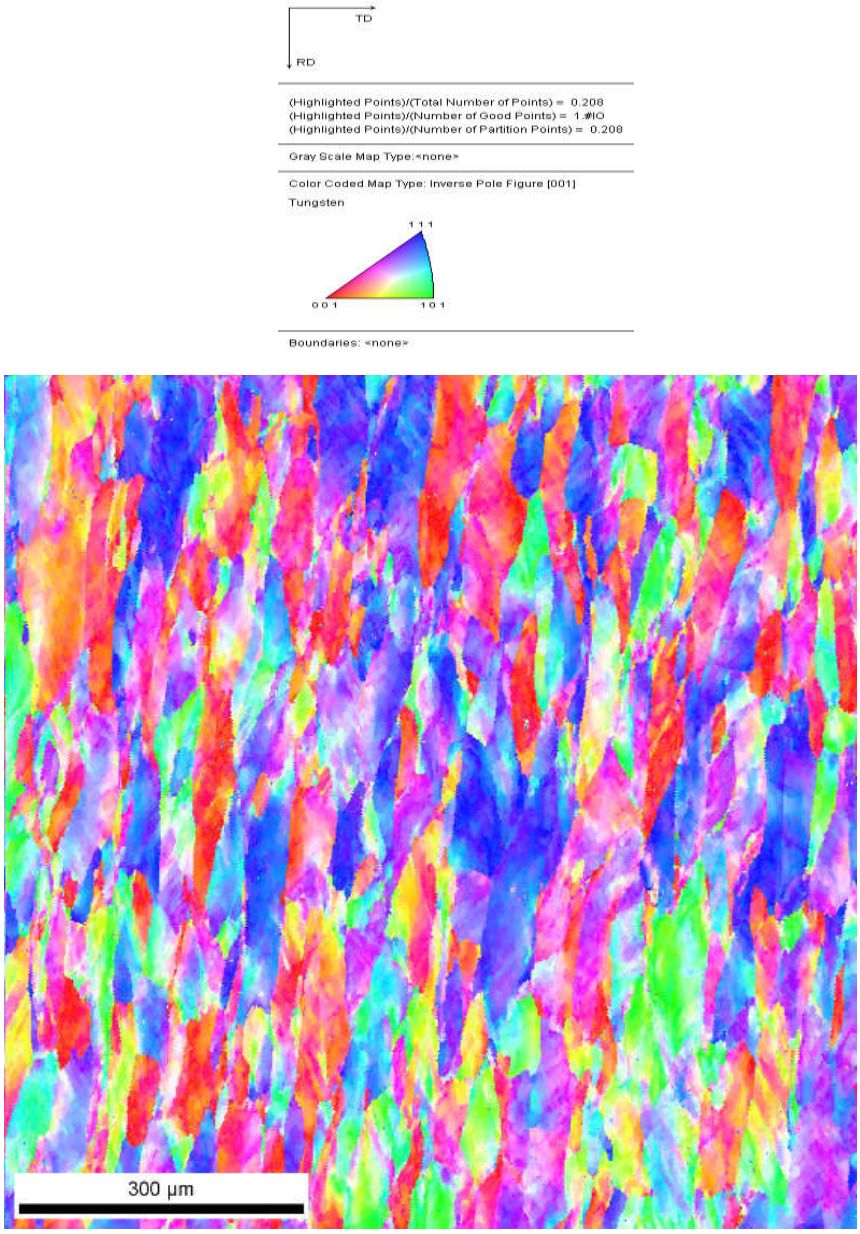

***Figure 15a**. Brick 6, LN section (rolling direction is vertical), midplane.*

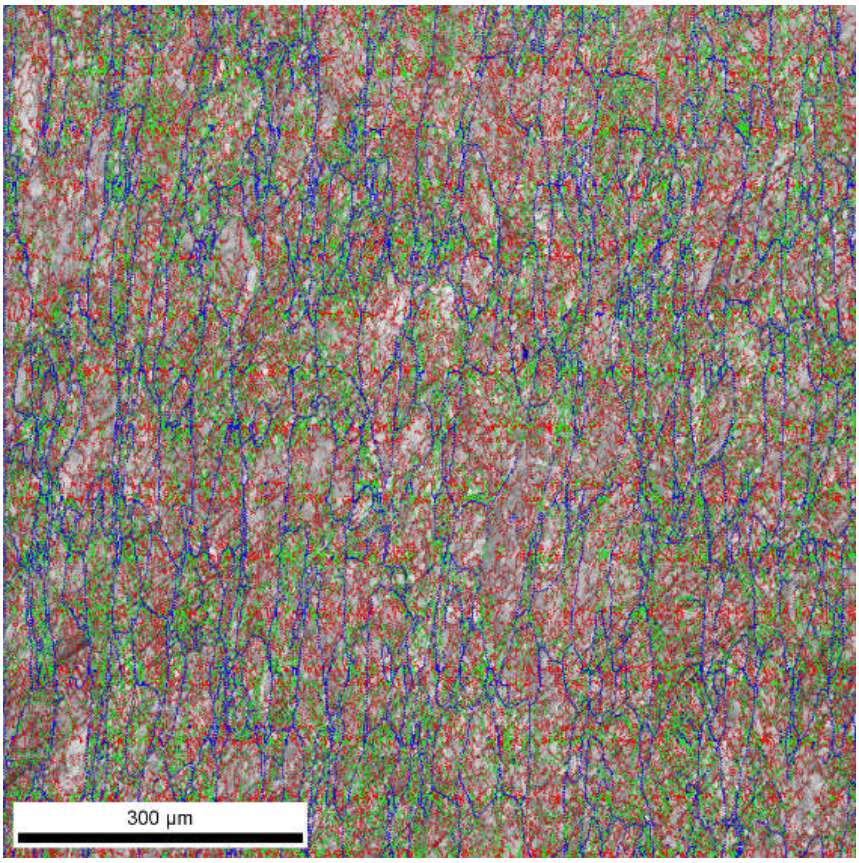

***Figure 15b**. Brick 6, LN section (rolling direction is vertical), midplane.*

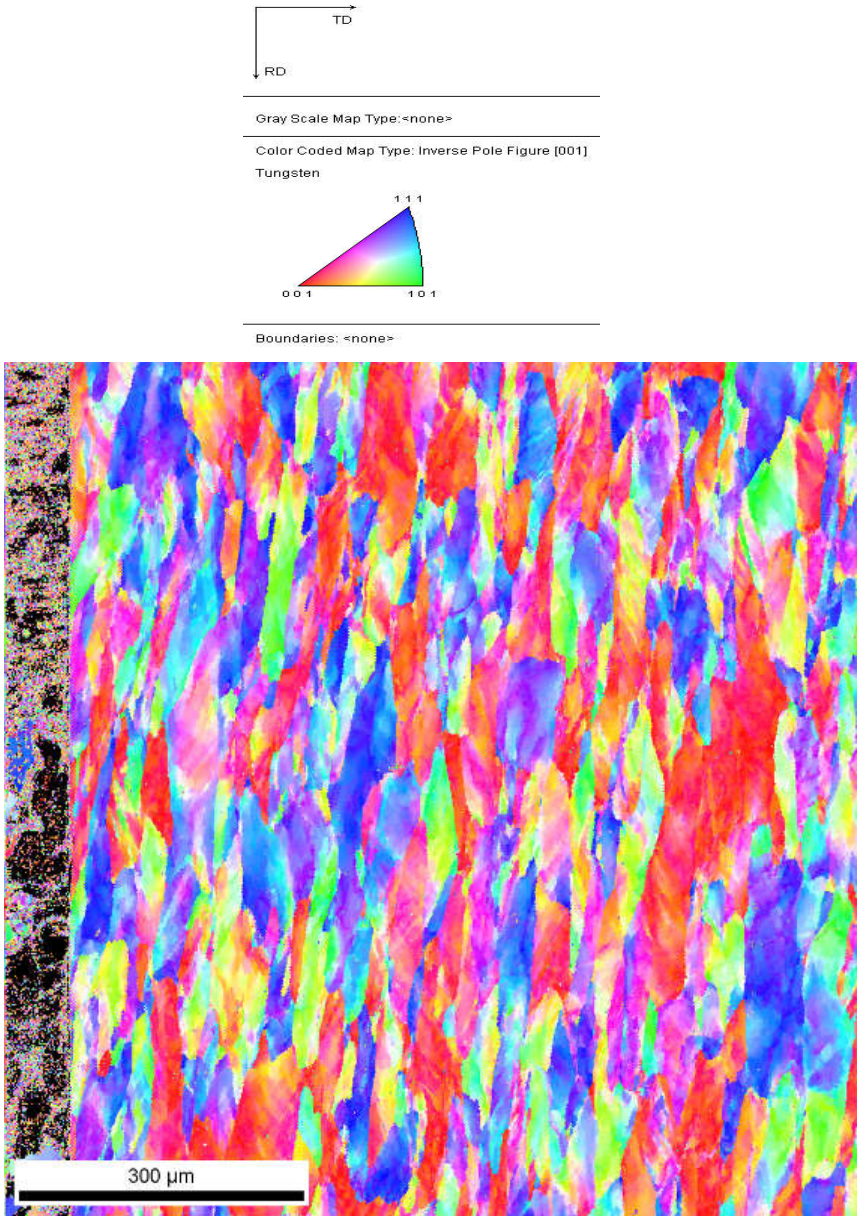

***Figure 15 c**. Brick 6, LN section (rolling direction is vertical), surface.*

Figure 15 d. *Brick 6, LN section (rolling direction is vertical), surface. Detail.*

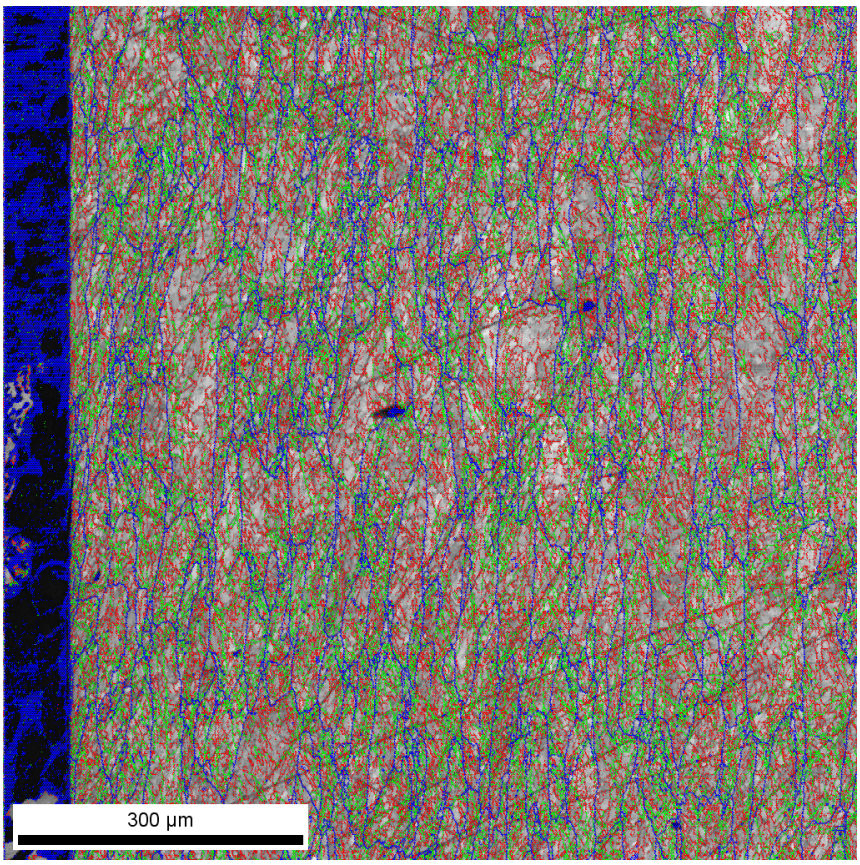

***Figure 15 e**. Brick 6, LN section (rolling direction is vertical), surface.*

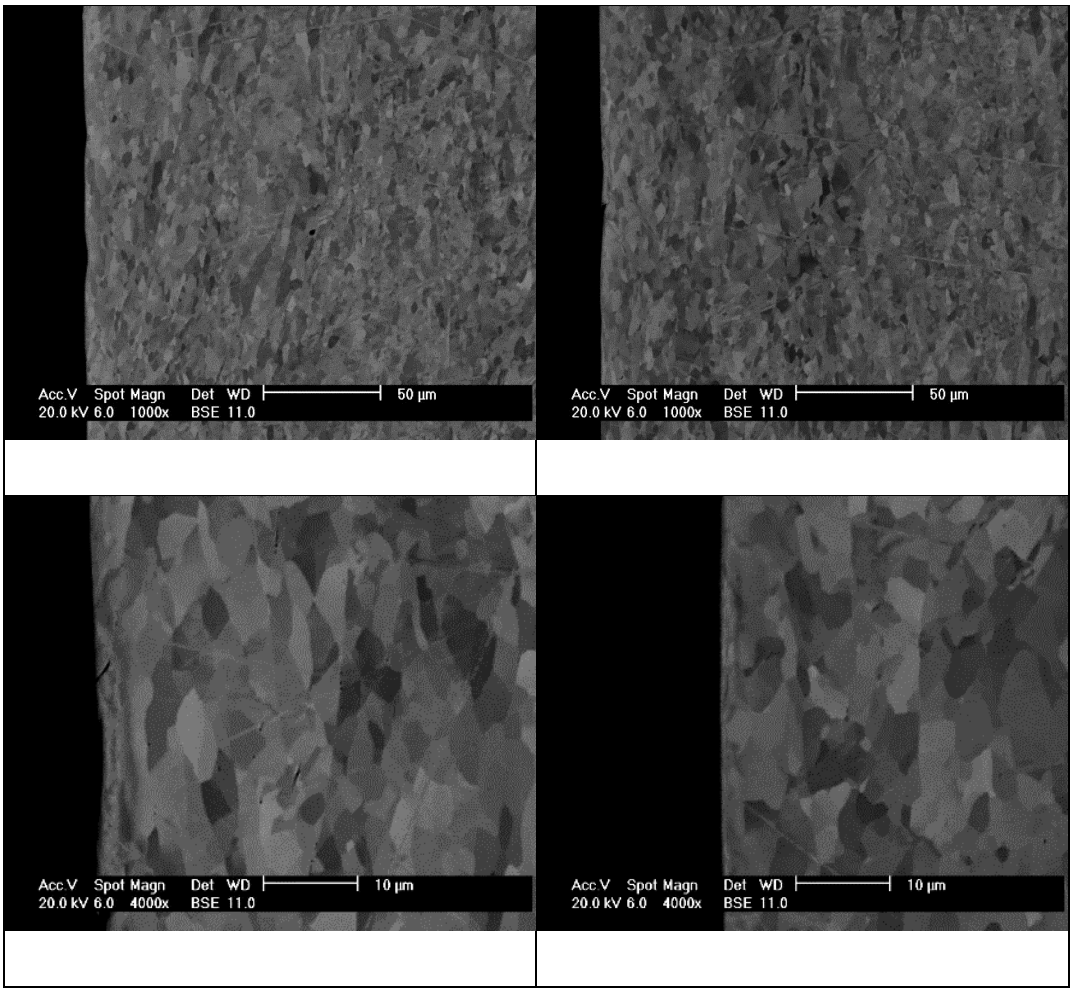

***Figure 16a**. BS-SEM images of the edge zone of brick 6, LN section. A heavily affected surface layer of about 3 µm is evident: severily deformed and with some (unfrequent) microcracks (of less than 2 µm).*

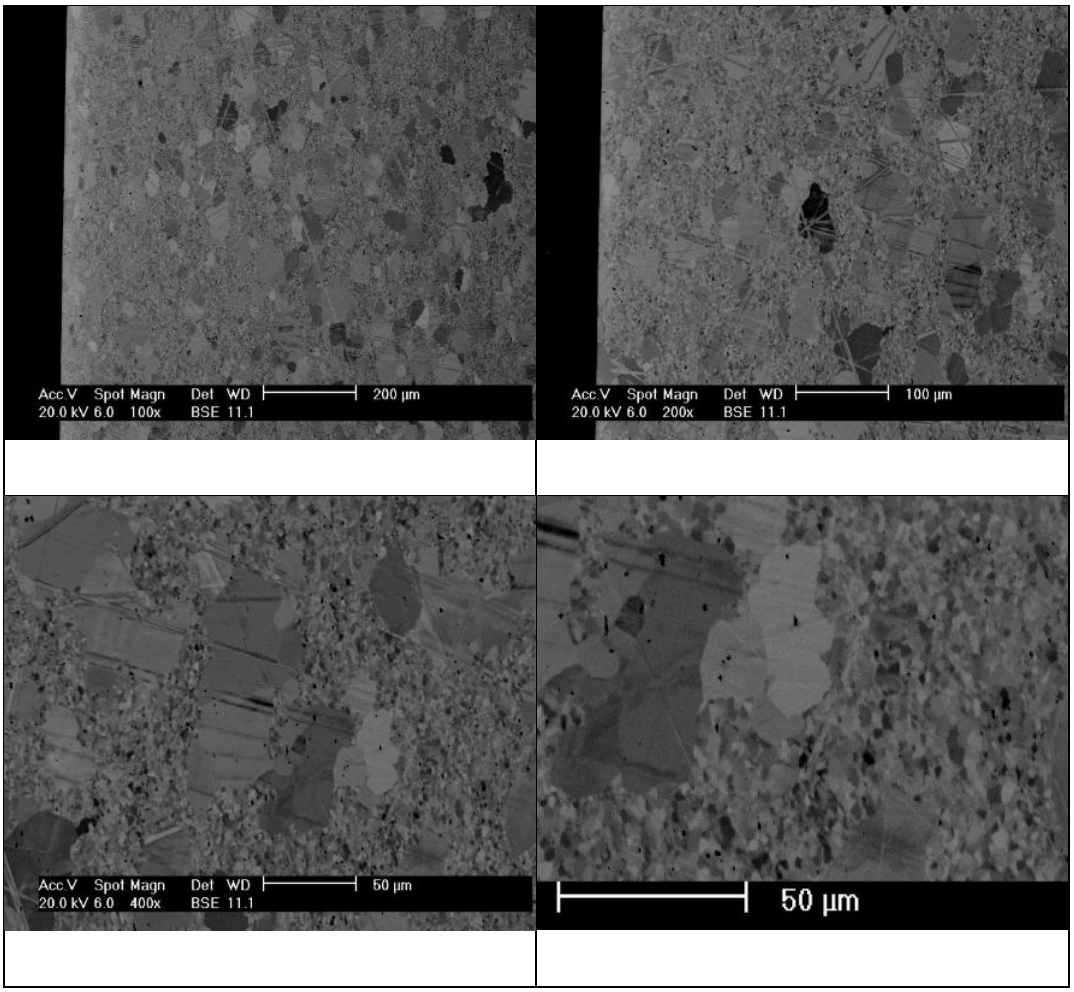

***Figure 16b**. BS-SEM images of the edge zone of brick 5N, LN section. No evidence of heavily deformed surface layer. Bimodal structure of grains free from substructure. The grain size of the fine fraction is very small.*

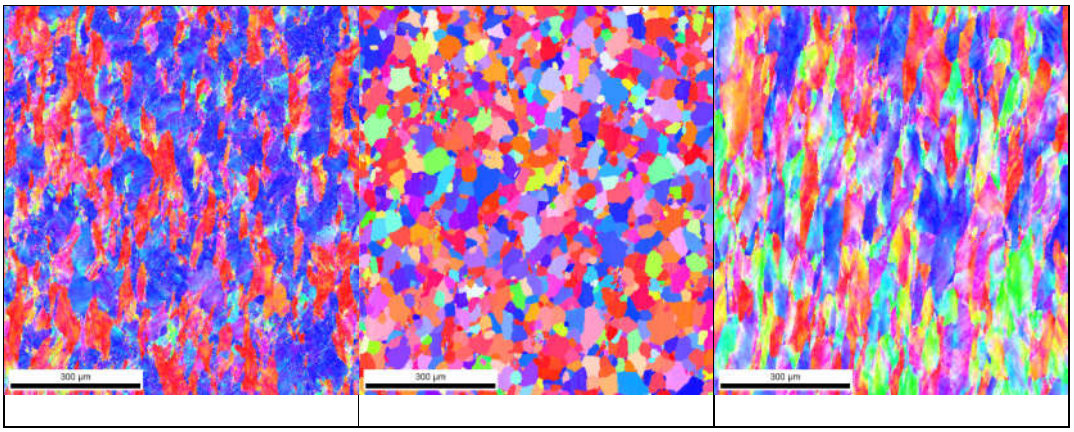

***Figure 17**. From left to right, bricks 2, 5N and 6, LN section, midplane.*

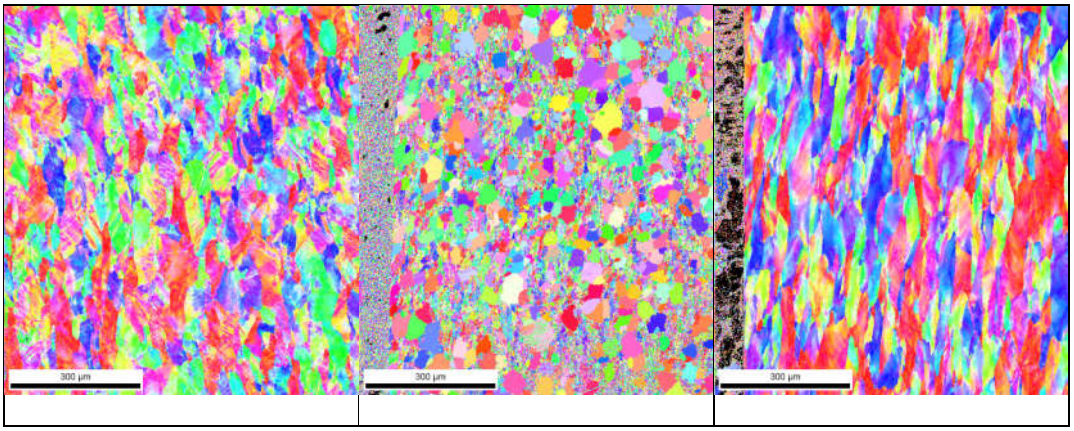

***Figure 18**. From left to right, bricks 2, 5N and 6, LN section, surface.*

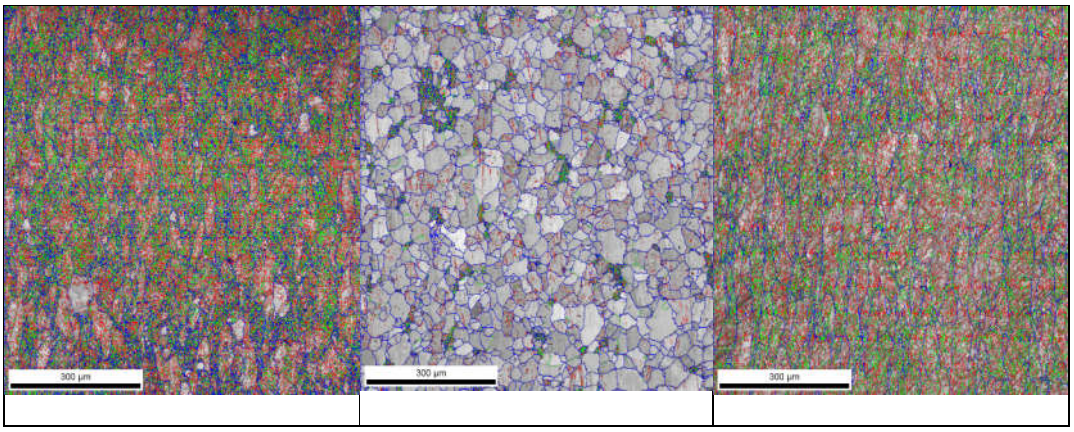

***Figure 19**. From left to right, bricks 2, 5 and 6, LN section, midplane, grain and subgrain boundaries superposed to image quality gray-scale.*

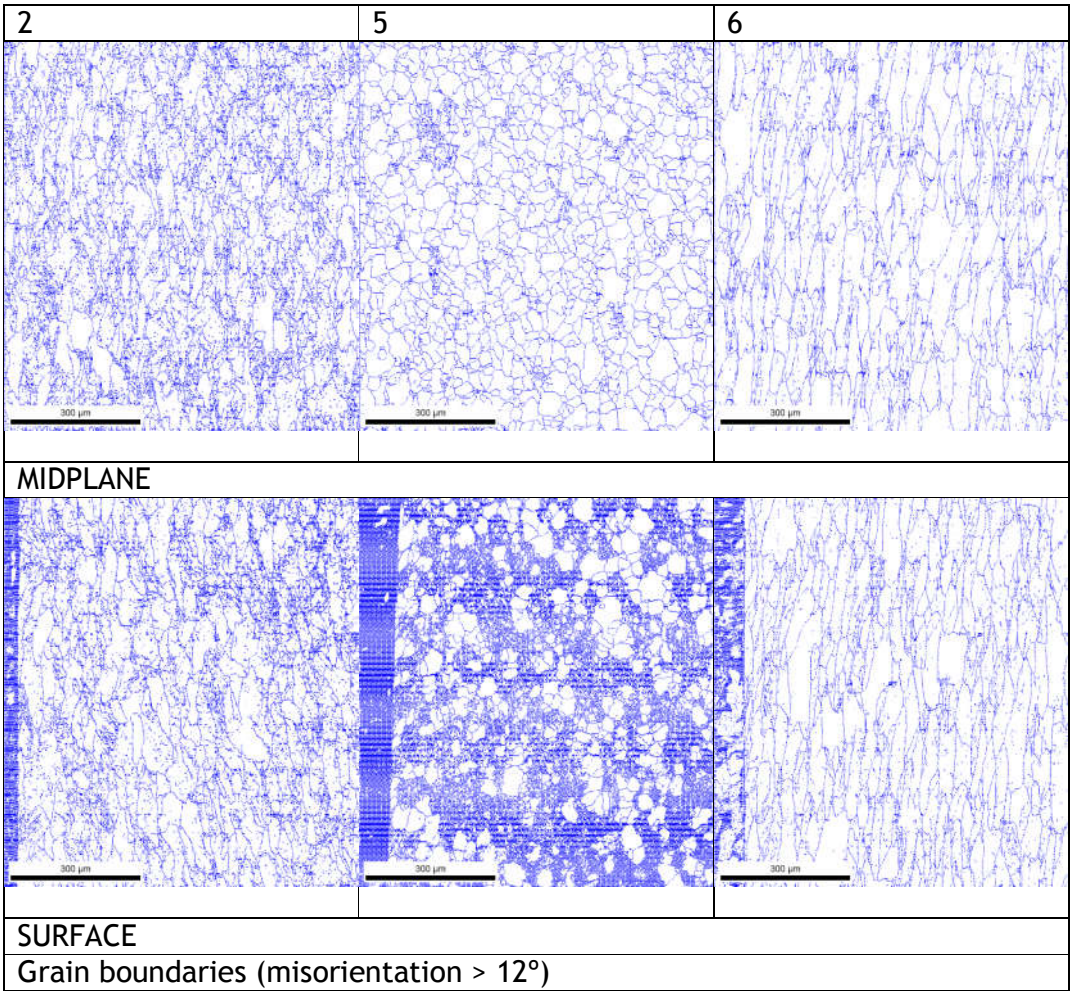

***Figure 20**. Comparison of grain sizes.*

Nº	MIDPLANE	SURFACE
2	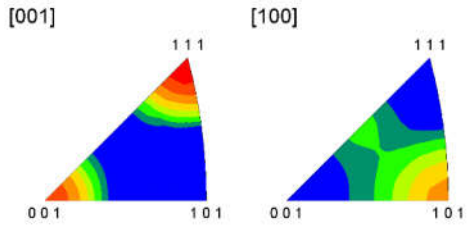	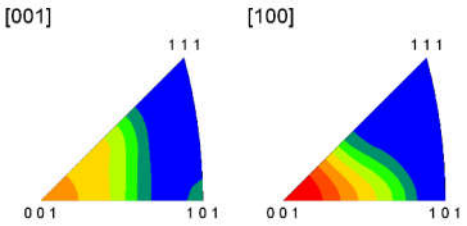
5 N	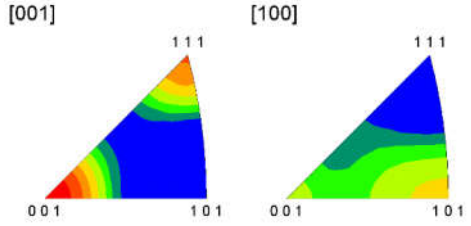	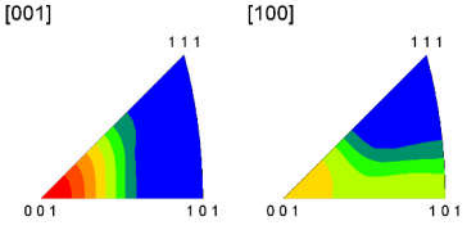
6	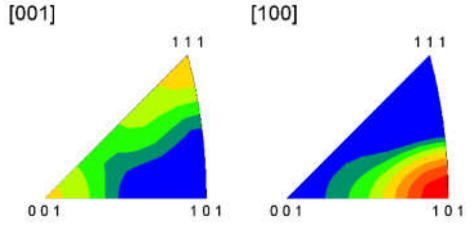	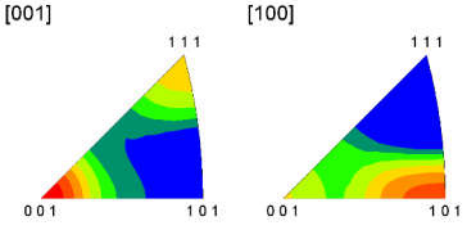
		***Figure 21**. Inverse pole figures (normal direction, [001] and rolling direction, [100]).*

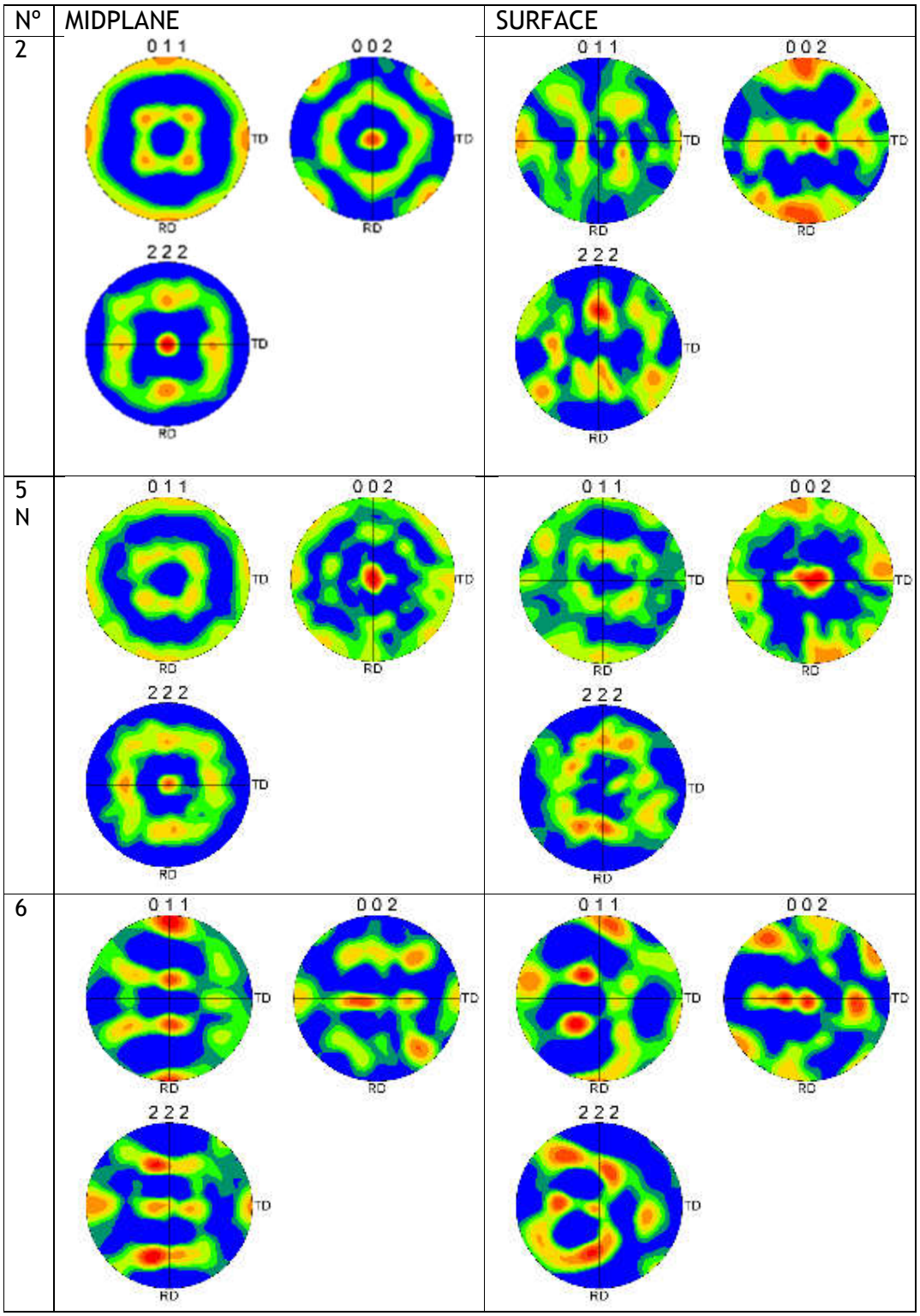

***Figure 22**. Direct pole figures, midplane and surface. The projection plane is the rolling plane.*

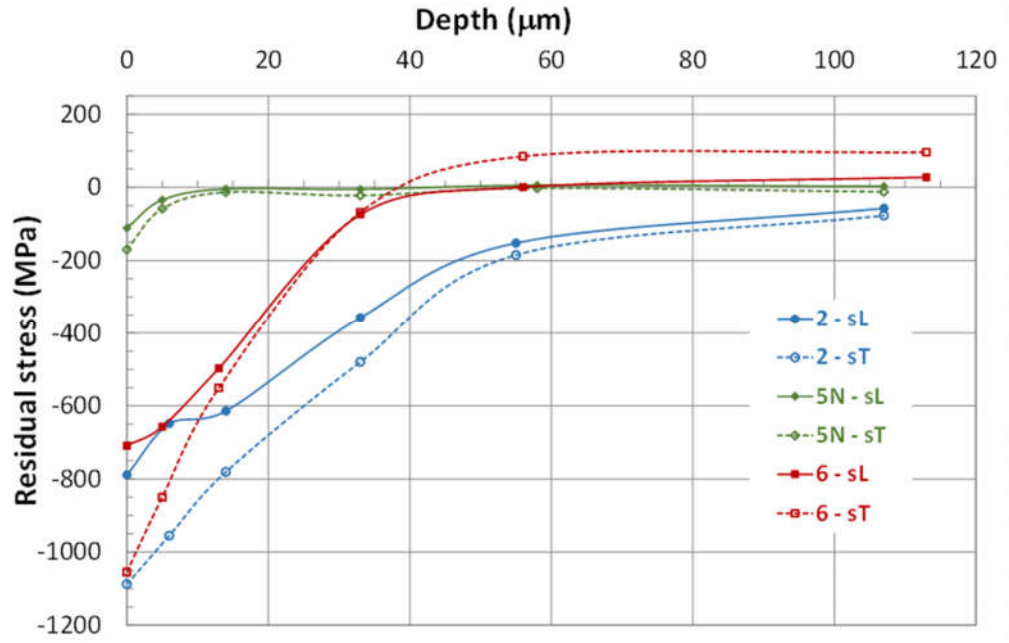

***Figure 23a**. Residual stresses measured in longitudinal and transverse directions on the rolling plane of the three bricks as a function of the sub-surface depth.*

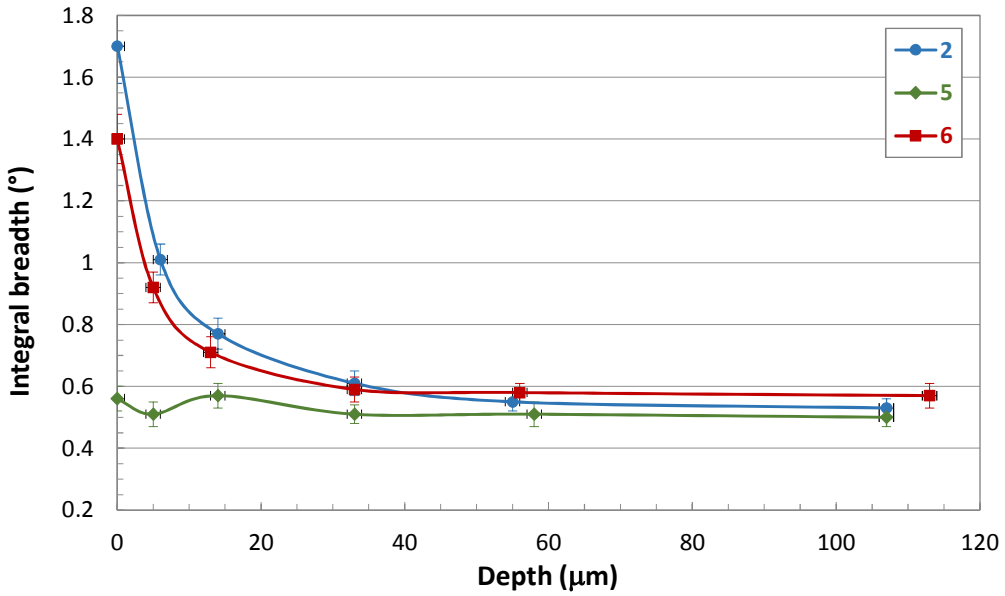

***Figure 23b**. Integral breadth (peak area/peak maximum height) vs. depth.*

Depth, nominal (μm)	2	5N	6
0	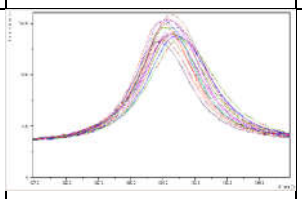	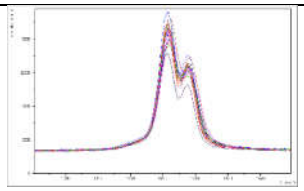	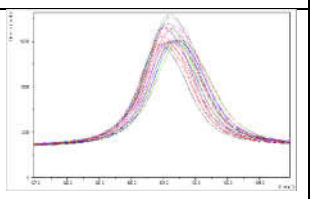
5	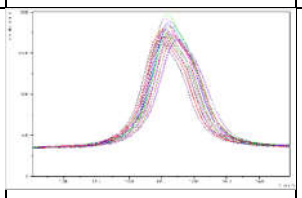	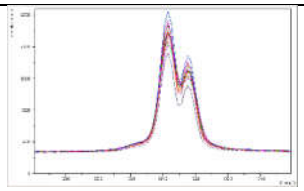	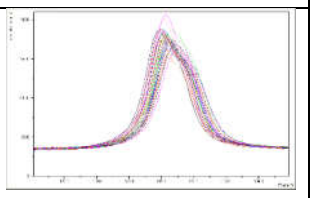
14	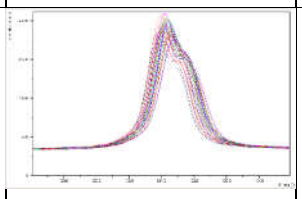	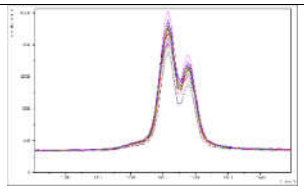	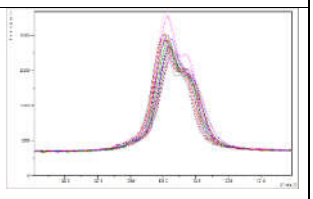
33	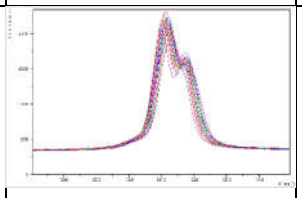	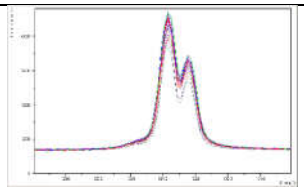	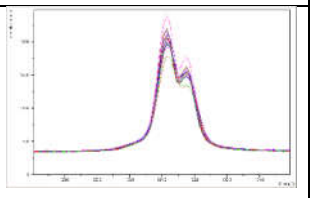
55	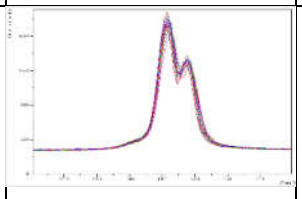	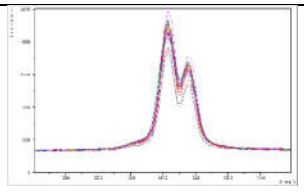	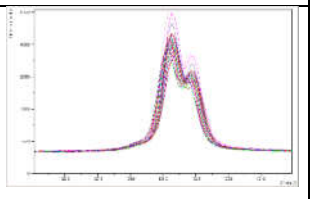
110	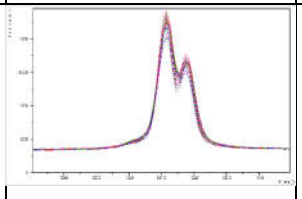	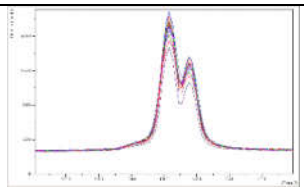	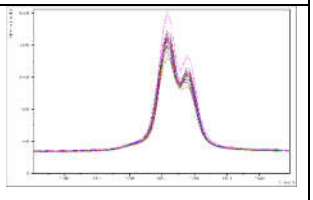

***Figure 24**. Diffraction peaks used for measurements of residual stresses on planes parallel to the rolling surface of bricks as a function of sub-surface depth. Measurement performed on lattice plane {321} using Cu Kα radiation (2θ = 131°).*

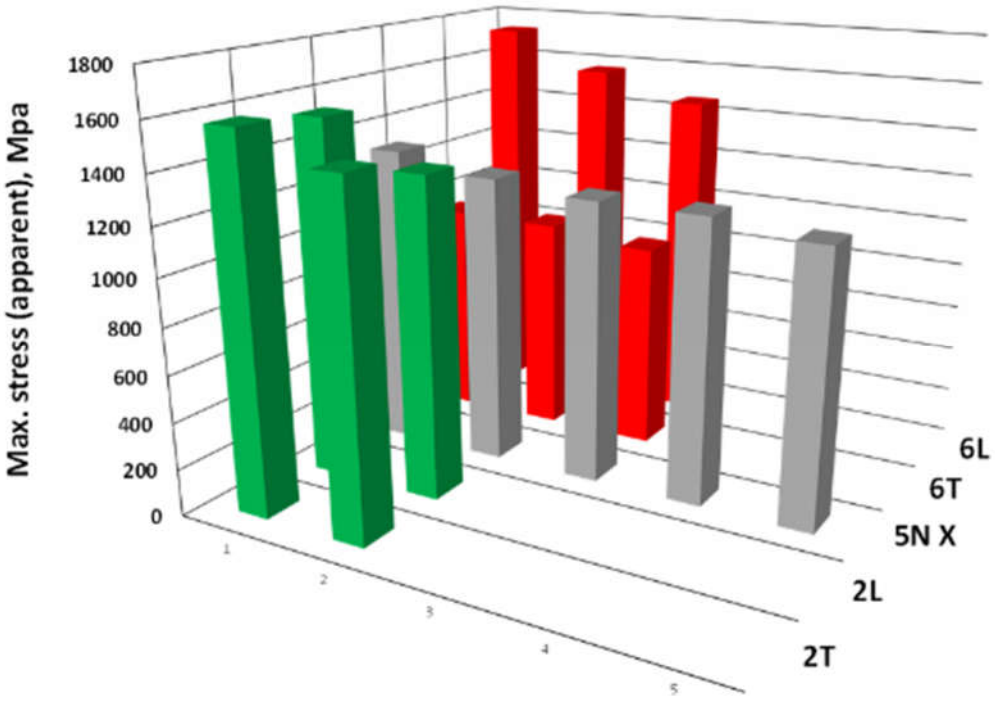

***Figure 25**. Maximum (apparent) tensile stress, three-point bending tests at 400°C in air, samples machined (EDM) from the surface of bricks 2, 5N and 6. Tensile stresses applied in longitudinal (L) or transverse (T) orientation, electro-discharge machined surface.*

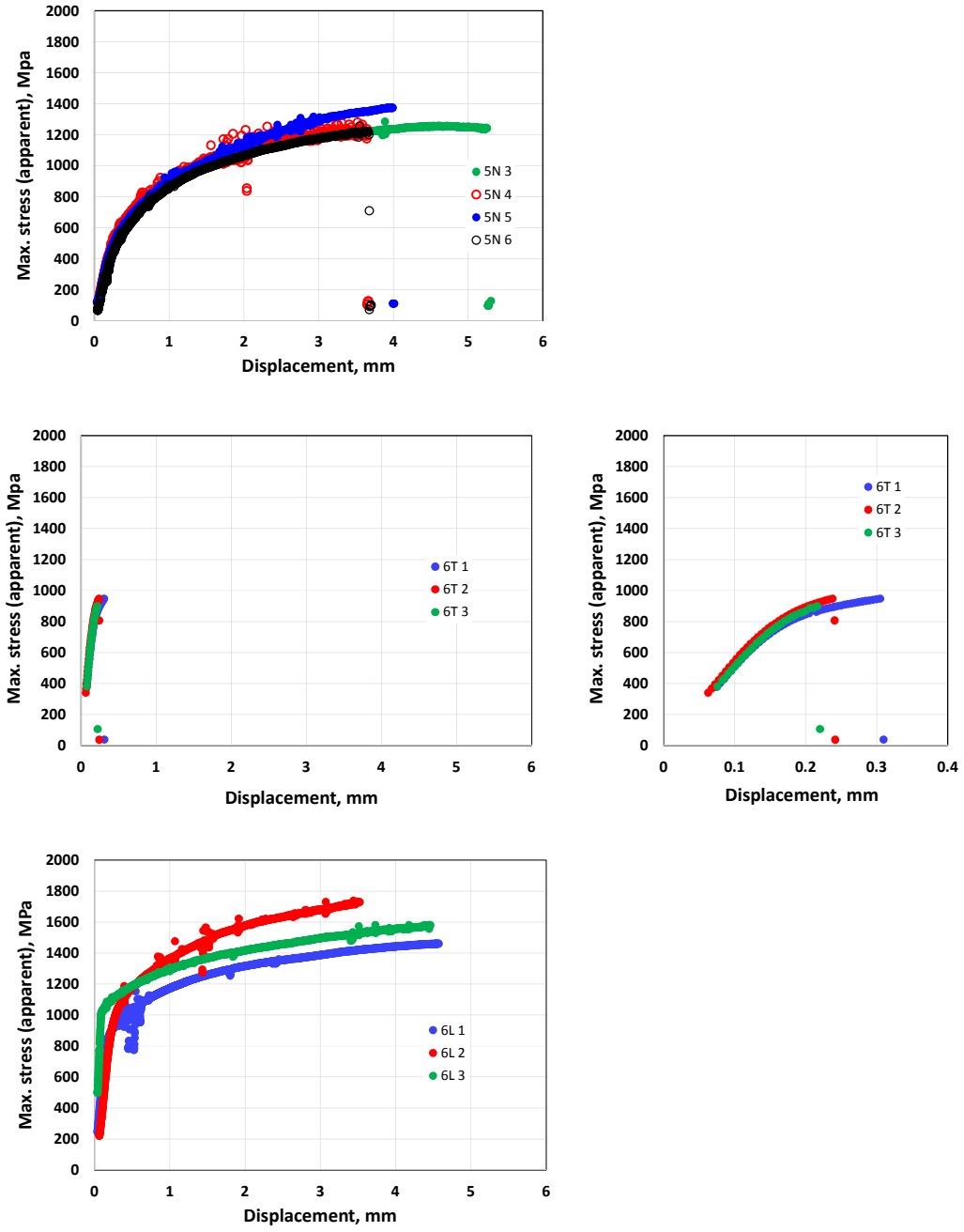

***Figure 26**. Apparent stress-strain behavior of bricks 5N and 6 at 400°C in air. Elastoplastic behavior and final brittle fracture. The zoom of the response of brick 6L shows that its behavior is elastoplastic too despite its small ductility.*

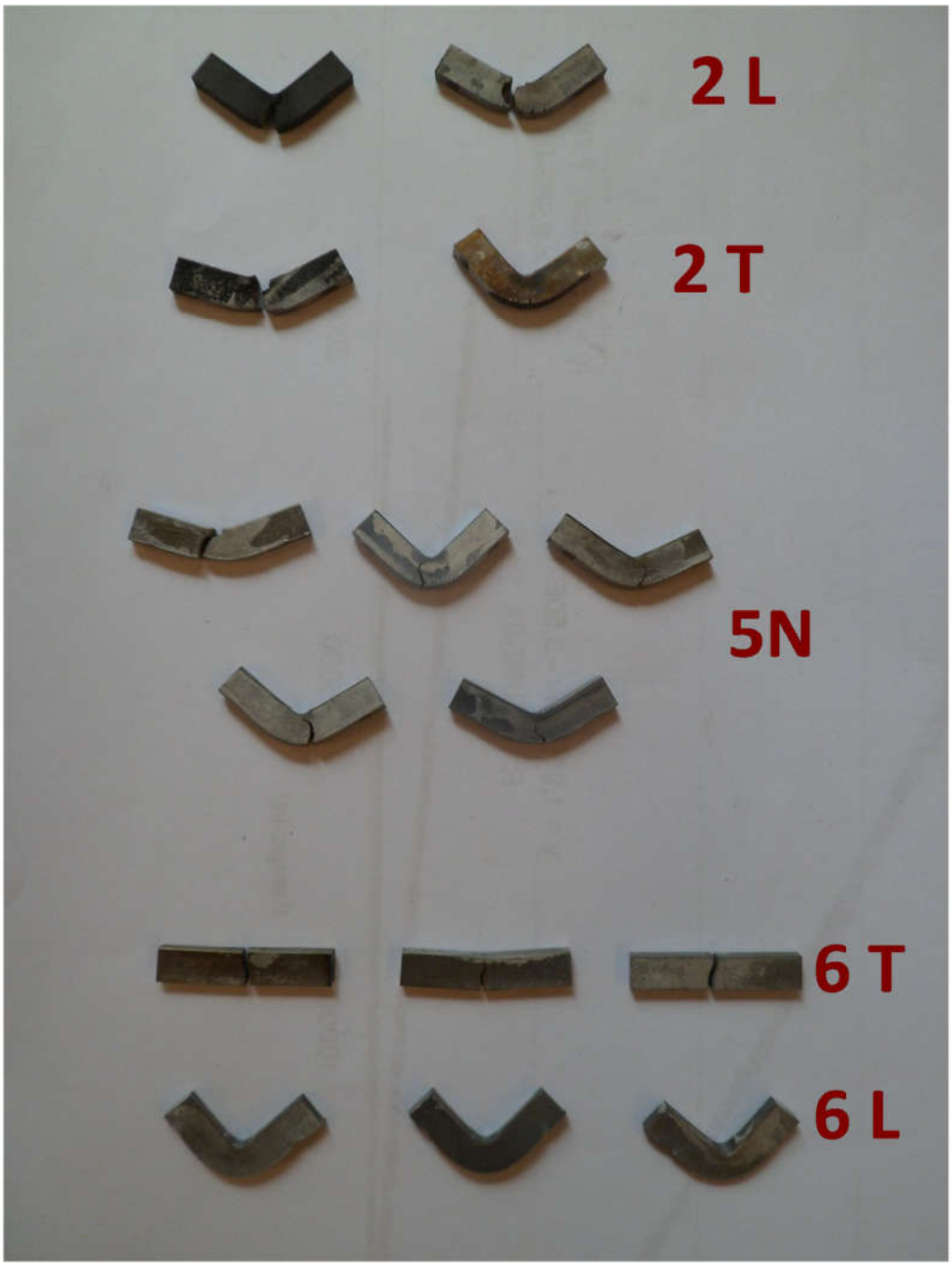

***Figure 27**. Bending tets, 400°C in air, broken specimens. The samples had been sprayed prior to testing with BN for protection and lubrication.*

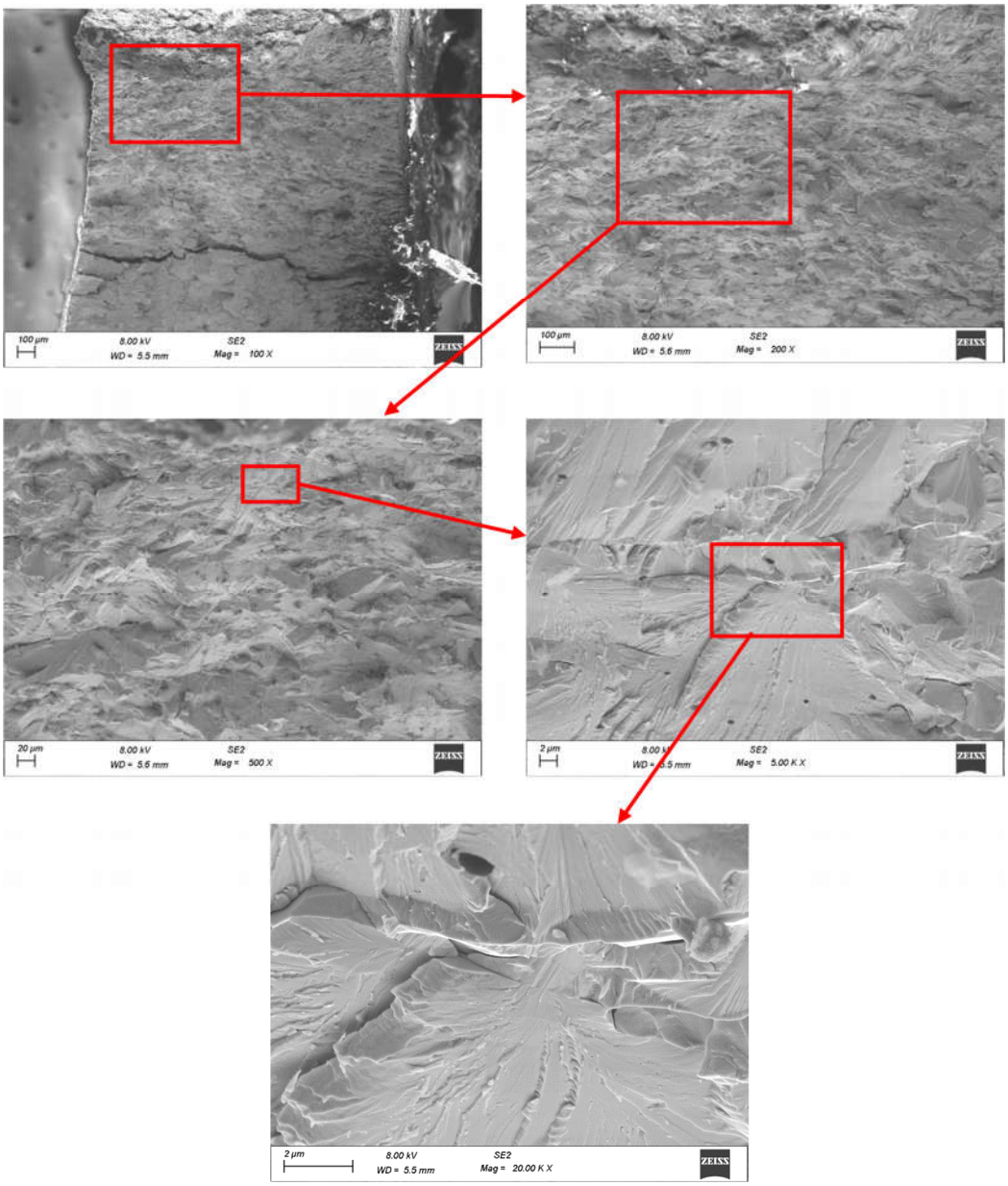

***Figure 28**. Fracture surface of sample 2 L (1). Direction T horizontal. Mainly distorted cleavage facets, small intergranular fracture surface fraction. Submicrometric pores.*

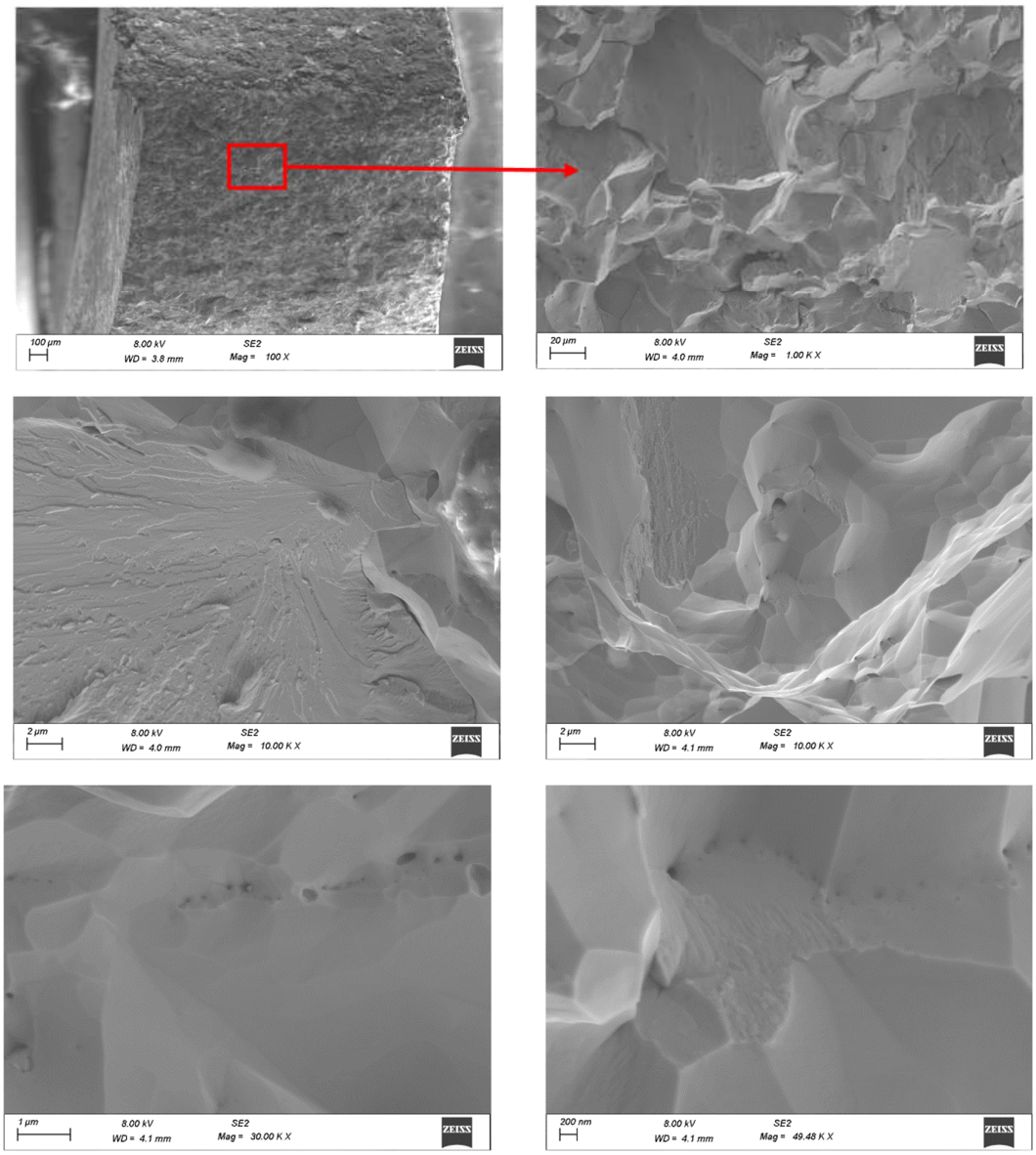

***Figure 29**. Fracture surface of sample 5N (problably T, L horizontal in the picture: some horizontal rows of pores). Large cleavage facets and regions of intergranular decohesion (fine grains).*

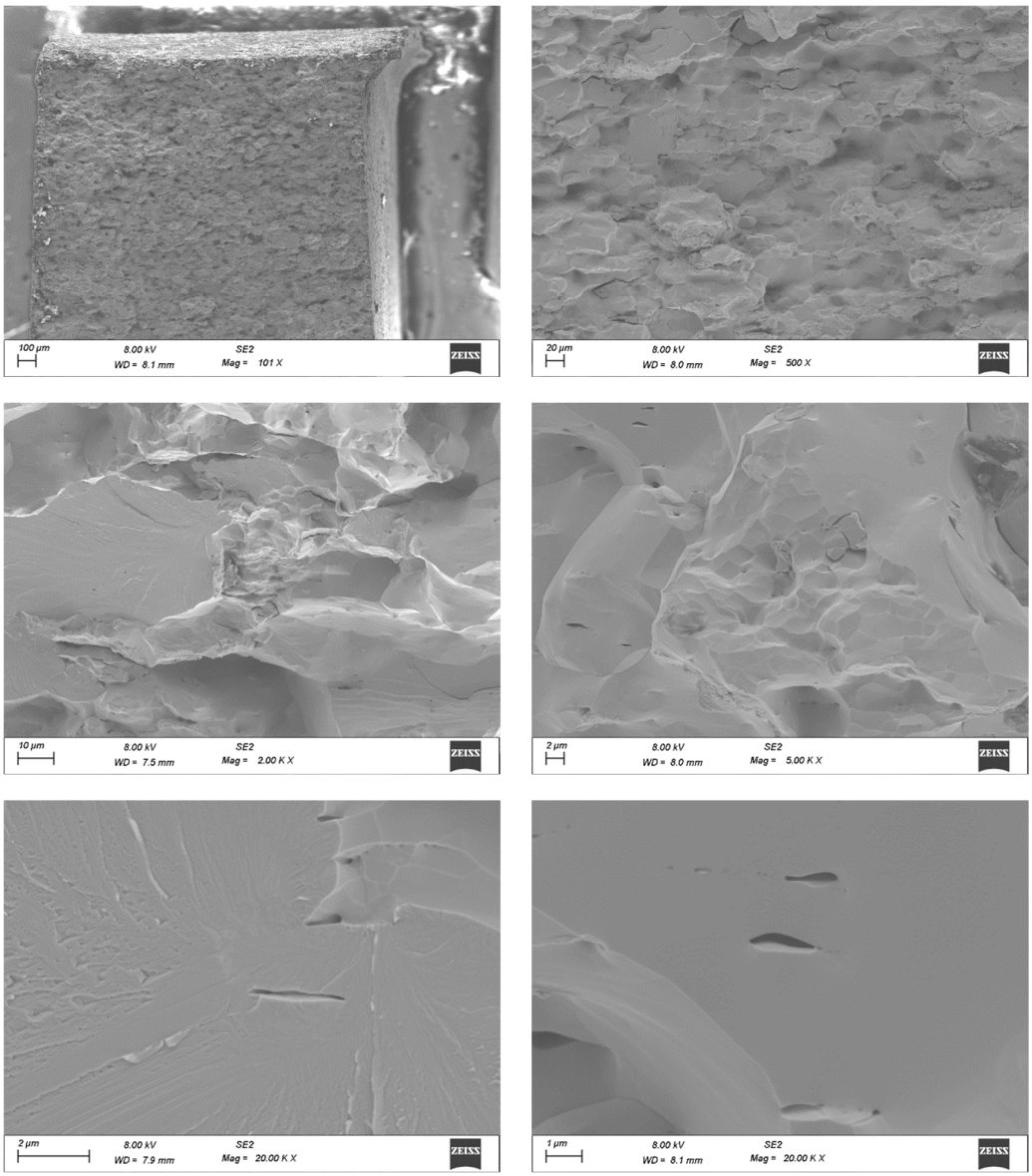

***Figure 30**. Fracture surface of sample 5N (problably direction T, L horizontal in the picture: some horizontal elongated pores). Large cleavage facets and regions of intergranular decohesion (fine grains).*

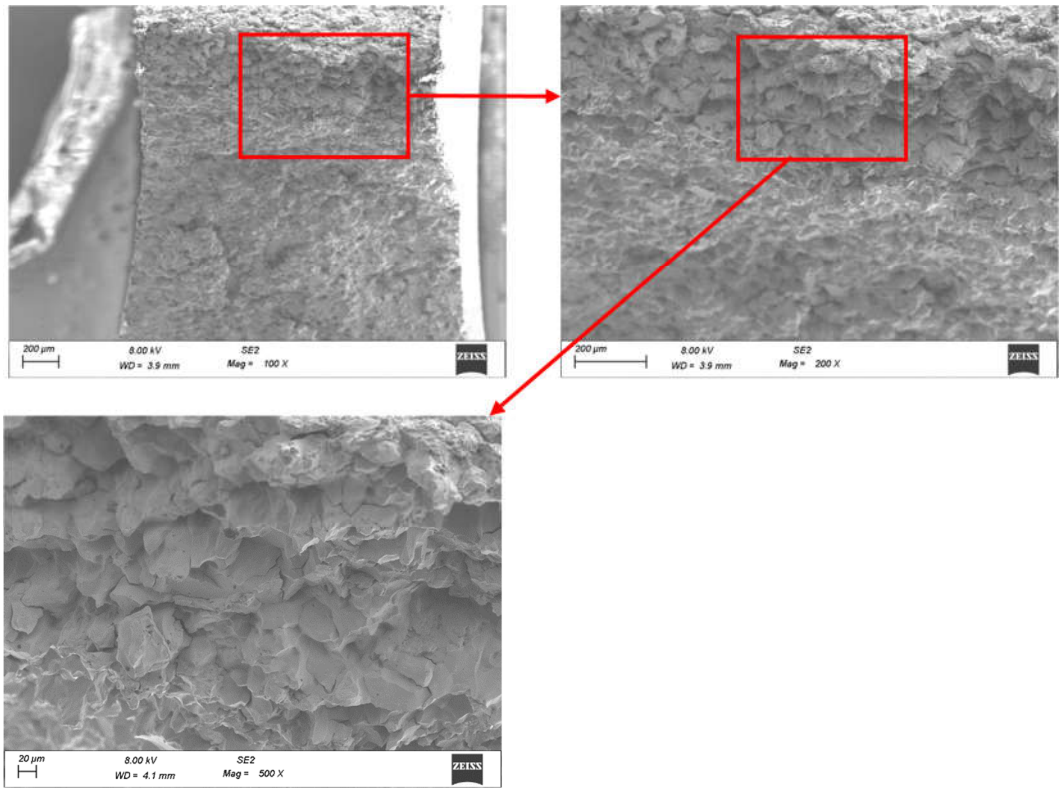

***Figure 31a**. Fracture surface of sample 6 T. Fracture initiation from the surface layer, (oxidized surface?, distorted cleavage?*

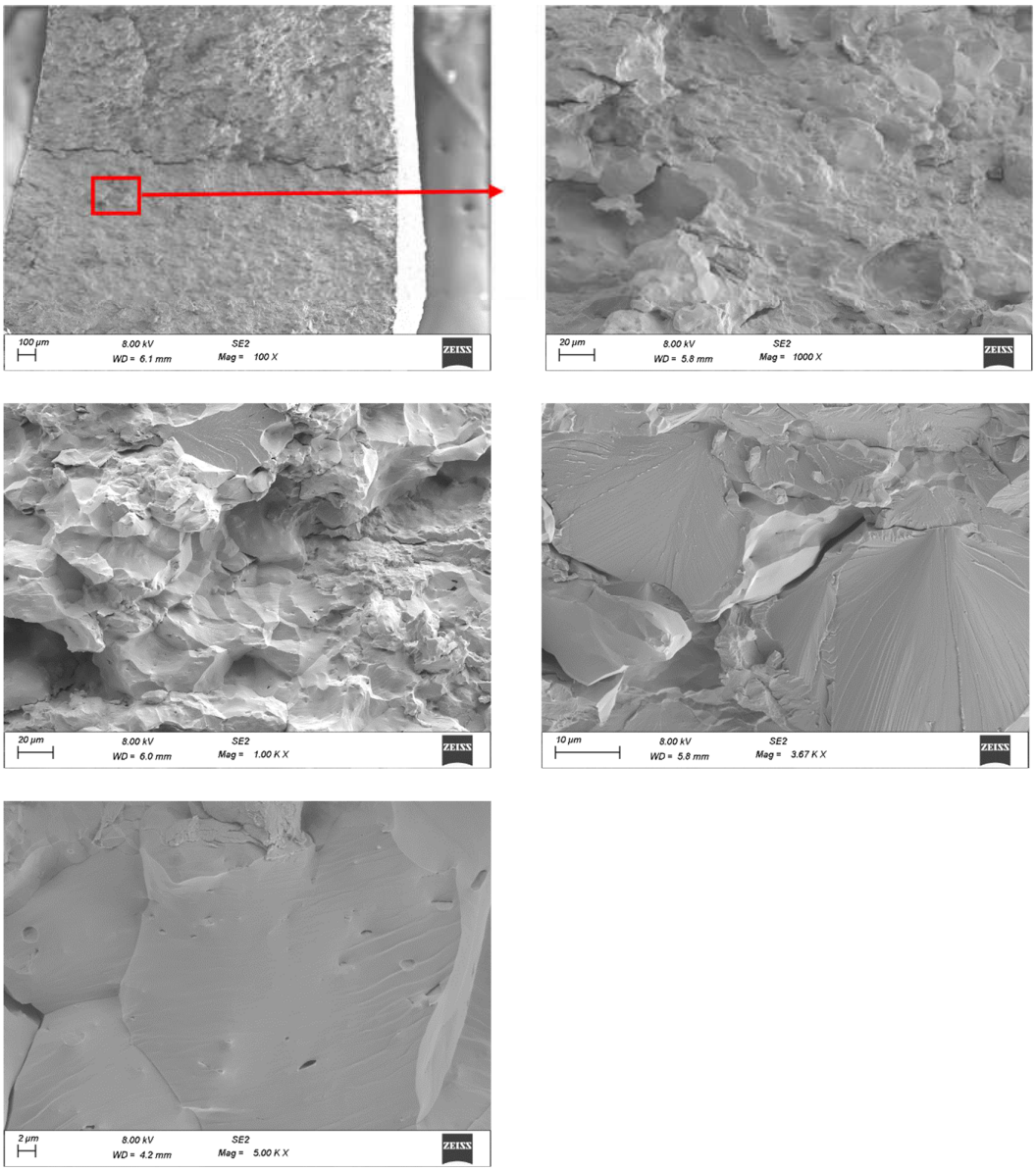

***Figure 31b**. Fracture surface of sample 6 T, away from the surface; L is horizontal; mixture of cleavage and intergranular decohesion.*

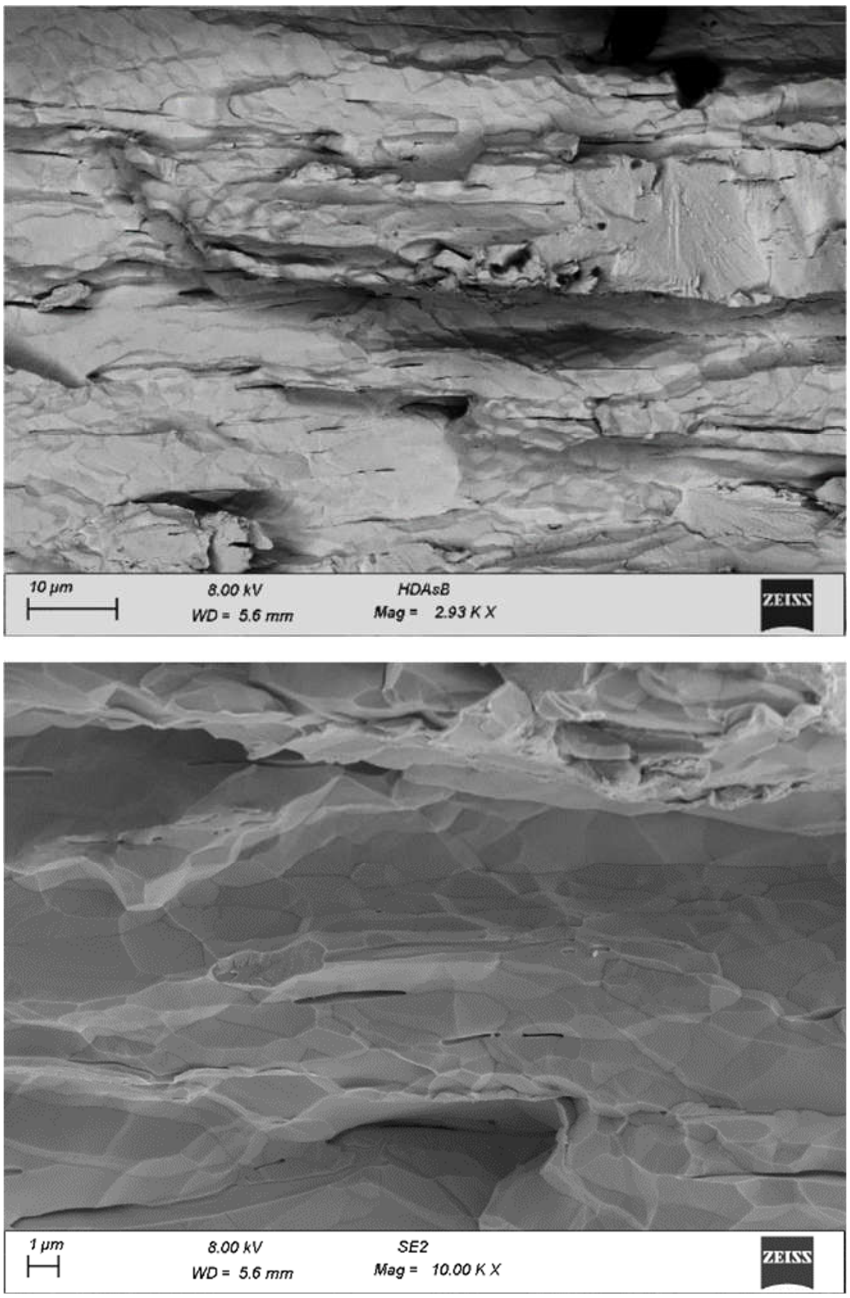

***Figure 32**. Fracture surface, sample 6 L. Distorted cleavage and intergranular decohesion.*

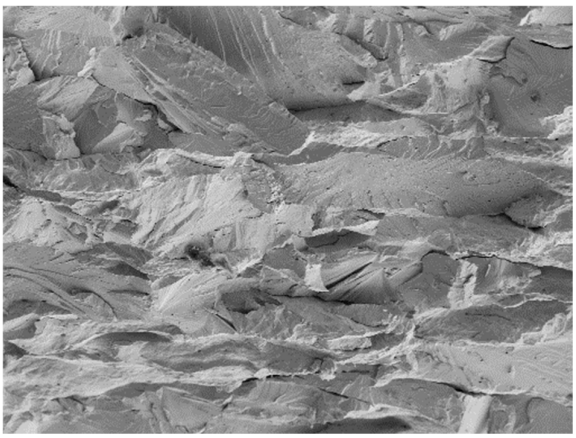

2 T

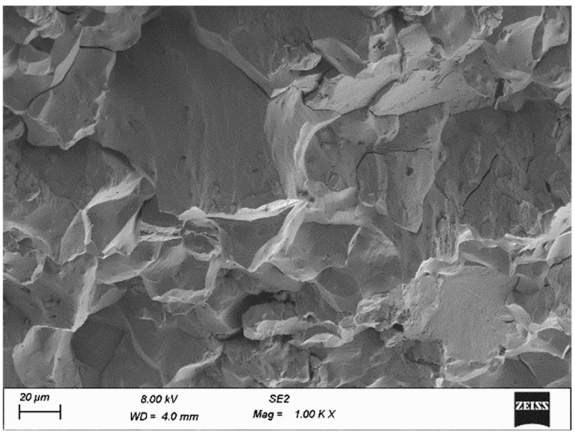

5N T

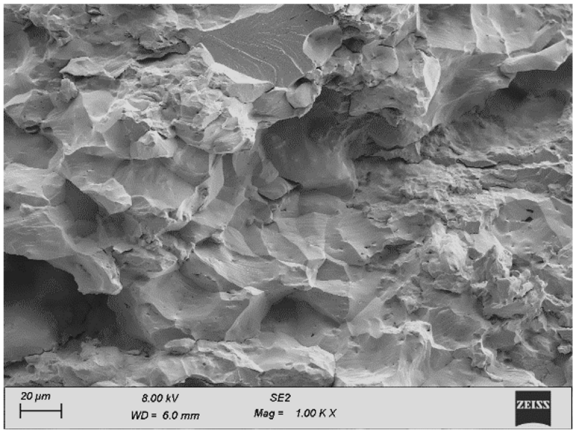

6 T

***Figure 33**. Comparison, same magnification. Direction L is horizontal, direction N is vertical.*

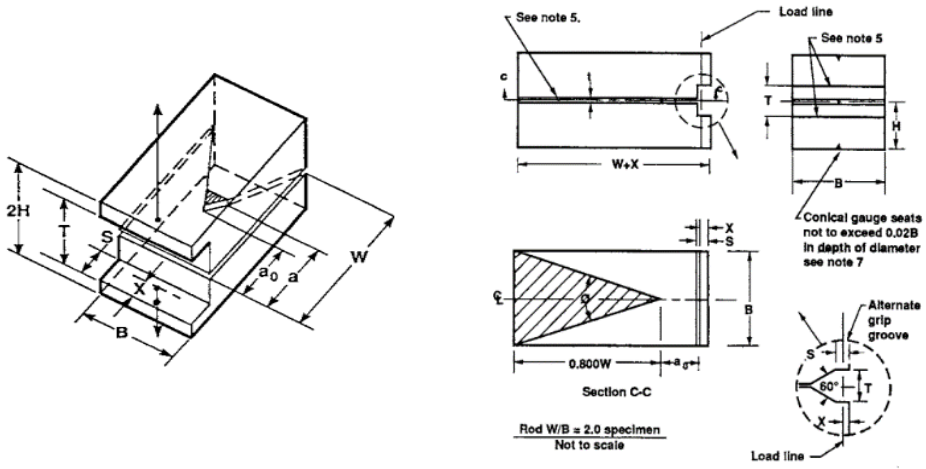

***Figure 34**.Chevron-notch fracture toughness sample. Upon loading, a crack starts stable growing from the notch apex until reaches a maximum of the opening force.*

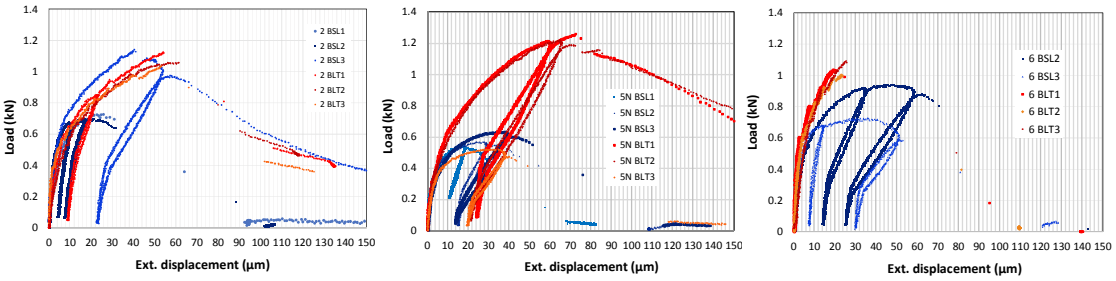

***Figure 35**. Load vs. mouth opening displacement, chevron-notch specimens, room temperature.*

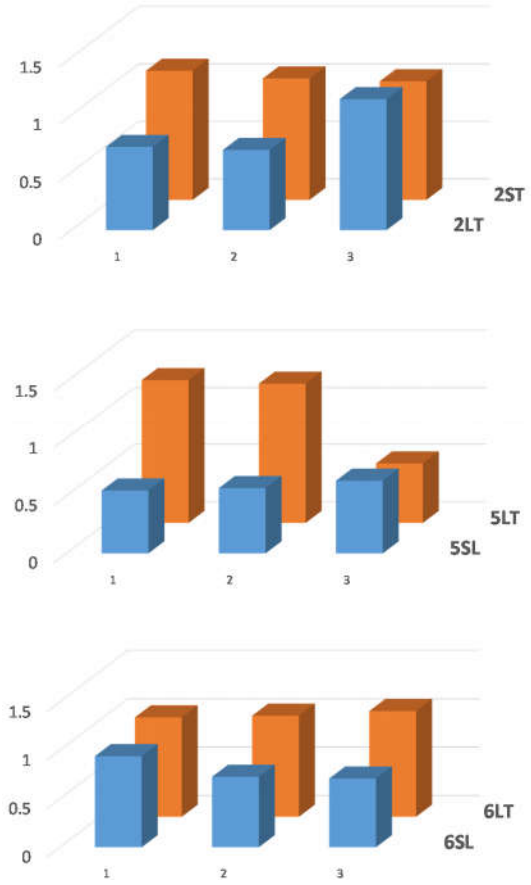

***Figure 36**. Maximum load (kN) in chevron-notch tests, room temperature.*

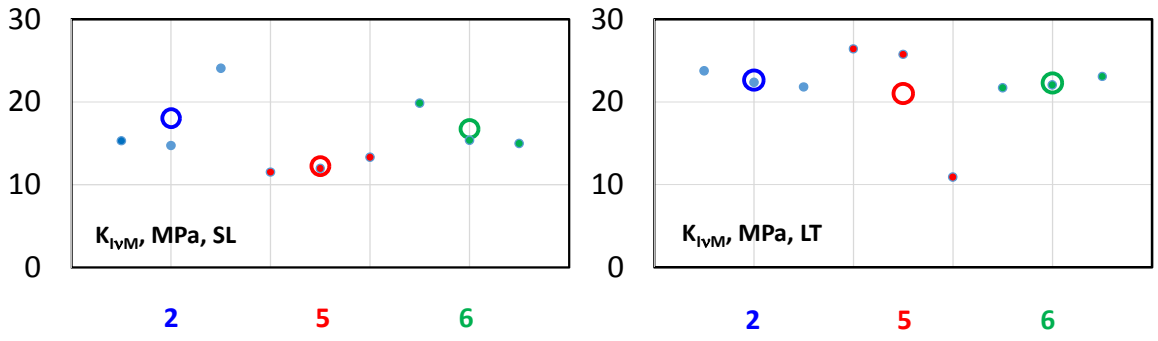

***Figure 37**. Plane-strain fracture toughness (crack propagation).*

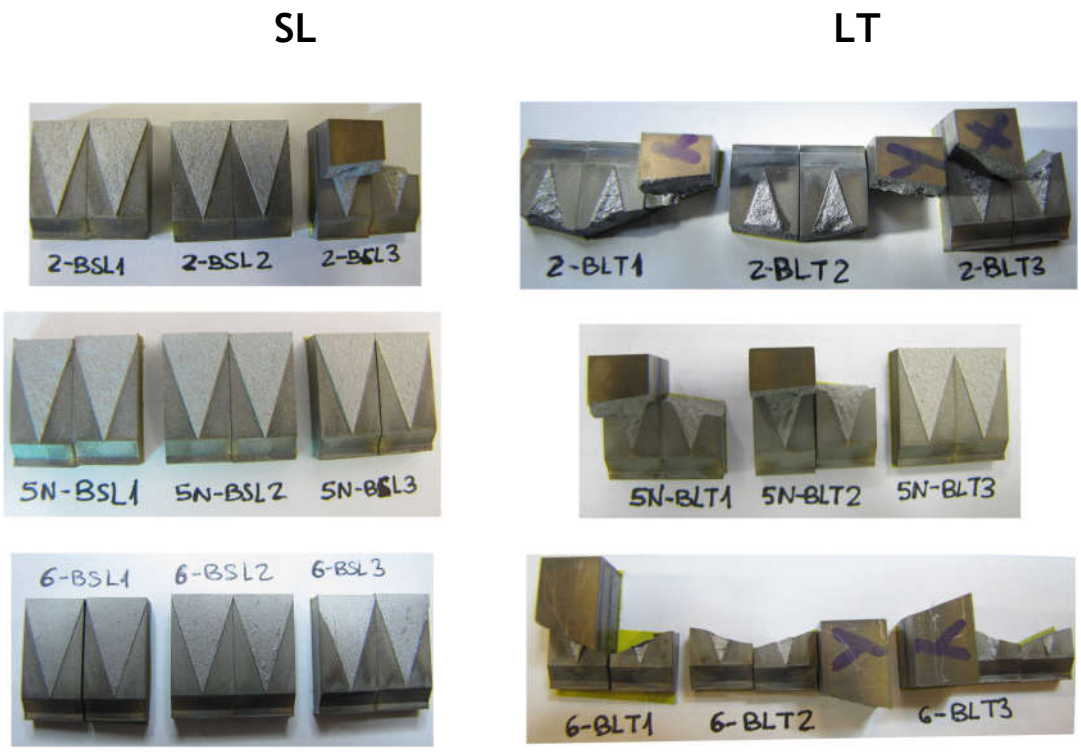

***Figure 38**. Fractured chevron-notch specimens.*